MEASUREMENT OF NEUTRON BACKGROUND IN KUO-SHENG NEUTRINO LABORATORY

A THESIS SUBMITTED TO
THE GRADUATE SCHOOL OF NATURAL AND APPLIED SCIENCES
OF
MIDDLE EAST TECHNICAL UNIVERSITY

BY

İHSAN OZAN YILDIRIM

IN PARTIAL FULFILLMENT OF THE REQUIREMENTS
FOR
THE DEGREE OF MASTER OF SCIENCE
IN
PHYSICS

FEBRUARY 2012

Approval of the thesis:

MEASUREMENT OF NEUTRON BACKGROUND IN KUO-SHENG NEUTRINO LABORATORY

submitted by **İHSAN OZAN YILDIRIM** in partial fulfillment of the requirements for the degree of **Master of Science in Physics Department, Middle East Technical University** by,

Prof. Dr. Canan Özgen _____
Dean, Graduate School of **Natural and Applied Sciences**

Prof. Dr. Mehmet Zeyrek _____
Head of Department, **Physics**

Prof. Dr. Mehmet Zeyrek _____
Supervisor, **Physics Department, METU**

Assoc. Prof. Dr. Muhammed Deniz _____
Co-supervisor, **Physics Department, KTU**

Examining Committee Members:

Prof. Dr. Müge Boz
Physics Engineering Department, Hacettepe University _____

Prof. Dr. Mehmet Zeyrek
Physics Department, METU _____

Prof. Dr. Selahattin Özdemir
Physics Department, METU _____

Prof. Dr. Altuğ Özpineci
Physics Department, METU _____

Assoc. Prof. Dr. Enver Bulur
Physics Department, METU _____

Date: _____

I hereby declare that all information in this document has been obtained and presented in accordance with academic rules and ethical conduct. I also declare that, as required by these rules and conduct, I have fully cited and referenced all material and results that are not original to this work.

Name, Last Name: İHSAN OZAN YILDIRIM

Signature :

ABSTRACT

MEASUREMENT OF NEUTRON BACKGROUND IN KUO-SHENG NEUTRINO LABORATORY

Yıldırım, İhsan Ozan
M.S., Department of Physics
Supervisor : Prof. Dr. Mehmet Zeyrek
Co-Supervisor : Assoc. Prof. Dr. Muhammed Deniz
FEBRUARY 2012, 60 pages

Particle physics experiments with low event rates highly depend on background suppression methods. Neutron component of the ambient background radiation is especially problematic since neutrons are difficult to shield directly. TEXONO collaboration has employed a hybrid neutron detector composed of two different scintillating materials to measure the neutron background directly in the Kuo-Sheng Neutrino Laboratory. Detector is operated after calibration and optimization studies and from collected data, neutron flux is obtained using computational methods.

Keywords: background, neutron, spectroscopy, scintillator, unfolding

ÖZ

KUO-SHENG NÖTRİNO LABORATUVARINDA NÖTRON ARTALANININ ÖLÇÜLMESİ

Yıldırım, İhsan Ozan
Yüksek Lisans, Fizik Bölümü
Tez Yöneticisi : Prof. Dr. Mehmet Zeyrek
Ortak Tez Yöneticisi : Doç. Dr. Muhammed Deniz

ŞUBAT 2012, 60 sayfa

Düşük sayım oranlı parçacık fiziği deneylerinde artalan bastırma yöntemleri önem taşımaktadır. Çevresel arkalan radyasyonunun nötron bileşeni, doğrudan yalıtmak güç olduğu için özellikle güçlük yaratmaktadır. TEXONO işbirliği, iki farklı sintilatör materyalini bir araya getiren melez bir nötron detektörünü Kuo-Sheng Nötrino Laboratuvarında nötron arkaplanını doğrudan ölçmek için kullanmıştır. Detektör optimizasyon ve kalibrasyon çalışmalarından sonra toplanan verilerden, bilgisayar temelli yöntemler kullanılarak nötron akısı hesaplanmıştır.

Anahtar Kelimeler: artalan, nötron, spektroskopi, sintilatör, ters evrişim

To my parents.

ACKNOWLEDGMENTS

I wish to thank to Prof. Dr. Henry Tsz-King Wong, who gave me the opportunity to work with TEXONO collaboration, where I gained most of my professional experience present.

I also wish to thank Prof. Dr. Mehmet Zeyrek, who encouraged and supported me in my field of research since my undergraduate years.

To Assoc. Prof. Dr. Muhammed Deniz, whose experiences I followed in my research in TEXONO, I owe a great debt for being supportive and patient throughout the path of this work.

I am thankful to my friends Mehmet Ali Olpak, Kıvılcım Vural, Taylan Takan, Deniz Olgu Devecioğu, and especially Selçuk Bilmiş and Sadi Başoğlu, for always being there at any time of need.

Finally, my parents, who never hesitated to support me on any decision throughout my entire educational life, deserves special thanks.

I would like to thank to Scientific and Technological Research Council of Turkey (TUBITAK) for the financial support during this study.

TABLE OF CONTENTS

LIST OF TABLES

TABLES

LIST OF FIGURES

FIGURES

CHAPTER 1

INTRODUCTION

TEXONO (Taiwan Experiment on Neutrino) is an experimental collaboration focusing on neutrino and dark matter research. Both areas of the experimental physics depend upon a detection sensitivity of very low count rates since interactions in consideration have very small interaction rates. Typical experiments based on direct detection of such interactions expect event rates of few counts per day, or for some dark matter studies researching annual modulation of galactic dark mater, few counts over the year can create crucial differences in the physics implications. Whatever detector technology is used in low count experiments, eliminating the background signals in data always constitutes a major part of such studies. Unfortunately, a complete isolation of radiation background is not possible even for very deep underground laboratories; however, there are various methods regarding the elimination of the background signals from desired data.

Neutron abundance in the background radiation environment has particular difficulties considering shielding of such particles or their interactions with typical low count detectors. With this scope, TEXONO employed a neutron detector to measure the exact amount of neutron radiation present in its experimental facility. This work gives a complete account of neutron background measurement carried out for the requirements of TEXONO.

Chapter 2 will discuss the characteristics of the radiation background. A complete list of possible environmental radiation sources and methods used to eliminate them will be tried to be given.

TEXONO will be introduced in the later Chapter 3 along with the characteristics of the neutron detector which was used for background measurement. This part will involve a description of the mentioned neutron detector and scintillation detection principles since is composed

of two scintillating materials as target. Using the theoretical information in this chapter, Chapter 4 will discuss the data analysis techniques.

Neutron spectroscopy (or dosimetry) with scintillation detectors has important application areas, but originally most of the techniques were initially developed for radiation protection purposes in the industrial facilities like nuclear reactors. For a particular detector reading in a radiation environment, several computational steps are necessary to obtain the implied neutron flux. These computational methods, including Monte Carlo calculations, will be given in Chapter 5. Results of the neutron flux calculations will follow in the later Chapter 6.

Final calculations of the neutron flux will later be used to estimate the background signals in the neutrino and dark matter measurements of TEXONO, but this part of the work is beyond the extent of this work.

CHAPTER 2

BACKGROUNDS TO PHYSICS EXPERIMENTS

Regarding the open questions in modern physics, it is not always possible to carry experiments designed in a way that measured signals are strong. Especially in the fields of experimental neutrino physics and dark matter physics, expected interaction rates for any kind of detector technology are very low and it is impossible to plan any research projects in these areas without considering the problem of filtering a weak signal out of background. These types of experiments are referred as low count rate, sensitive or rare event experiments and there is a large cumulation of background suppression techniques developed to make such studies possible. On the other hand, even in the deep underground laboratories, a complete isolation of background radiation is not possible.

A variety of detector technologies are available that are suitable for low count experiments, differing from gram scale target mass germanium detectors to tonne scale Cerenkov counters. However, all are based on ionization detection of the secondary particles induced by rare process in consideration, and in this manner, they are not readily distinguishable from any background event [1].

Typical expected event rates for neutrino and dark matter experiments are in the range of 10^{-4} – 10^{-1} counts per day. Sensitivity to these numbers can only be achieved by proper shielding and background subtraction techniques in underground laboratories.

Taiwan Experiment on Neutrino (TEXONO) is also a sensitive experiment. Research topics of the collaboration include reactor neutrino studies and dark matter physics based on Ge detector technologies. Group already have an experience of background studies from its reactor neutrino laboratory.

2.1 BACKGROUND SOURCES

Most dark matter experiments are located in deep underground laboratories, since cosmic rays are the strongest source of background radiation. However, even in deep underground, a complete isolation is not possible, and environmental component of background remains similar. To estimate the amount of the background and to decide on the optimal laboratory design, background sources should be well understood. Sources can be classified under four main categories.

- 1. Natural radioactivity of radionuclides present in the environment.
- 2. Radioactivity of impurities in the detector and the shielding materials.
- 3. Radioactivity induced by cosmic rays upon their interactions with pure materials of detector and shielding components and surroundings.
- 4. Direct interactions of secondary cosmic rays with the detector.

First category, radionuclides present in the environment may be primordial (radioactive elements present in the earth since its formation) or anthropogenic (man made). Products of their decay chains may include gamma rays, neutrons, α and β particles. Since this radiation is produced outside of the detector system, charged component can be ignored since they are easily shielded. On the other hand, γ rays and neutrons need special attention. Most abundant radioactive isotopes are ^{238}U, ^{232}Th, ^{40}K and ^{87}Rb. Rubidium decays by β emission and does not create background problems. Average concentrations of the other isotopes in an average rock sample is given in table 2.1.

Table 2.1: Concentrations of primordial radionuclides in the average rock [2].

Isotope	Concentration ($Bq \times kg^{-1}$)
^{238}U	36
^{232}Th	44
^{40}K	800

Unit $Bq \times kg^{-1}$ indicates the number of decays by isotopes contained in 1 kg of rock. Numbers correspond to an emission of 10 photons $cm^{-2}s^{-1}$ from the surface of the rock [2] requiring thick lead shielding.

^{222}Rn, a member of uranium and thorium decay chains, creates special problems. Under normal conditions, radon is in gas form. As it is generated by uranium and thorium, it diffuses through the rock and into the air causing airborne radioactivity. Daughters of radon later may saturate and stick to the detector and shielding parts causing long term contamination if the air inside the experimental areas is not cleaned.

Environmental neutron background results from uranium and thorium either by their spontaneous fission (only ^{238}U) or by (α, n) reactions. Latter one is much more dominant, in which an α from the decay chain of uranium or thorium is captured by another element emitting a neutron. Certain naturally abundant isotopes of elements in the composition of terrestrial rock like beryllium, carbon, oxygen, calcium, magnesium has high α-capture rates and contribute greatly to the fast neutron background [3].

Radioactivity from impurities of detector and shielding materials is similar to the environmental sources. First of all, since shielding materials are obtained by mining, uranium, thorium and potassium are also present in these in small concentrations. Amount of the background neutrons, in this case, is related to the α capture rate of the material. In addition to the uranium and thorium, shielding and detector parts are also contaminated by their less abundant radioisotopes. ^{210}Pb in lead can be given as an example.

Both for rock and shielding materials like copper, lead, iron/steel, expected (α, n) neutron fluxes have been calculated by Tomasello et al. using the known concentrations and by using Monte Carlo techniques [4]. Energy distribution of these neutrons are between 1-8 MeV with a peak at around 1 MeV.

Cosmic ray induced background is the reason for carrying low count experiments in deep underground laboratories. At sea level, without any shielding, most intense cosmic rays components are muons and neutrons. Neutrons have short mean path length and are easily attenuated. Even if the laboratory is not underground, building structures are enough to reduce the strength of the cosmic neutrons below that of environmental neutrons. On the other hand, muons has very long attenuation lengths. It is not the direct interactions of muons with detector that constitute a background problem but induced radioactivity from their interactions with shielding parts and environment close to the detector. Muon induced neutrons and radioisotopes contribute to the detector background. Muon induced neutron background, in contrast to the environmental, is harder, i.e. energy spectrum extends to GeV level, even though the

total flux is lower than the environmental one [5]. Induced radioisotopes are only a problem if they are generated in the target mass of the detector, otherwise their decay products are easily shielded.

Increasing the amount of shielding to reduce the muon induced neutron background is not a solution since the shielding material will only be effective for induced radiation without substantially lowering the muon flux. Hence more shielding material means more target material for muons to interact resulting in similar amounts muon induced neutrons. This is why underground laboratories are preferred [3]. Total muon induced neutron flux estimated for a 2 km deep underground site is in the order of $10^{-10}\ cm^{-2}\ s^{-1}$ [5] which is negligible compared to environmental sources.

Direct interaction of cosmic muons with detector is a problem if it results in a radioactive isotope. Especially for Ge detectors, it is possible to observe characteristic gamma energies of the radioisotopes induced by the muon interactions with the target material of the detector [2, 3].

2.2 BACKGROUND SUPPRESSION METHODS

First level of suppressing the background is through optimal usage of shielding. Lead and copper are the best options due to their stopping power, but their contribution to the background environment still remains, as described in the last section. In a comparison, lead has more stopping power and copper has higher radiopurity. Hence, lead is a better alternative to be used in the outer layers of the shielding. Then copper can be used as the innermost shielding. In general, a boron loaded polyethylene layer is used for neutron shielding since C and H has high interaction probabilities with fast neutrons and B is a very efficient slow neutron absorber. This layer can be placed as outer layer if the experiment site is underground, muon flux is low and only neutron background is environmental.

Background can be further suppressed by rejecting the background events using anti-coincidence detectors which operates simultaneously with the main detector. Detector arrays that will entirely cover the main detector are efficient in reducing the cosmic ray induced background since muon induced events are generally associated with showers of multiple particles. In TEXONO, main Ge detector is operated with a plastic scintillator array and a NaI(Tl) scintil-

lation detector. Both Ge and NaI(Tl), which is used as anti-Compton veto detector, have high gamma detection efficiencies through Compton scattering. A NaI(Tl) detector that entirely covers the Ge target mass also suppresses the background from muon induced radioactivity in Ge, since cosmogenic radioisotope production is accompanied by gamma emission. In this case, emitted gamma ray will most probably trigger the NaI(Tl) too.

Other background suppression methods are based on subtracting the measured or calculated background signal from data. Reactor neutrino studies of TEXONO has the opportunity to measure the background since there are periods when the reactor is not operating. Moreover, if the composition of the background sources are known, background signal in the detector can be simulated for subtraction [6, 7, 8, 9, 10]. However, they require a complete understanding of the sources and configuration of the surroundings. This work, by measuring the neutron background separately, will help the estimation of the background signals after simulating the measured neutron flux for Ge detectors in use.

CHAPTER 3

EXPERIMENTAL TECHNIQUES

Texono is a low threshold low energy experimental particle physics collaboration located in Academia Sinica in Taiwan. Until now, collaboration has reported results on standard model parameters, beyond the standard model expectations and dark matter physics using their measurements with various detectors including a CsI(Tl) crystal array and different variations of germanium semiconductor detectors.

Main experimental facility of TEXONO is Kuo-Sheng Neutrino Laboratory (KSNL) located inside the Kuo-Sheng Nuclear Power Plant in the northern region of Taiwan. Group is also planning to carry underground measurements in Jin-Ping Underground Laboratory which is located in the Sichuan Province of China. The laboratory construction is mostly over and it is the deepest underground laboratory to carry dark matter and other key physics researches.

KSNL is primarily designed to conduct reactor neutrino measurements through neutrino-electron scattering since reactors are rich sources of electron antineutrinos. The laboratory is at 28 meters distance away from the reactor core which has 2.9 GW nominal thermal output producing an $\bar{\nu}_e$ flux of $6.4{\times}10^{12}$ cm^{-2}s^{-2} at the neutrino laboratory.

3.1 PREVIOUS STUDIES OF TEXONO BASED ON KSNL MEASUREMENTS

TEXONO published a series of physics results on standard model related to $\bar{\nu}_e$ - e scattering, as well as beyond the standard model theories and dark matter physics based on their measurements. Until now, measurements has been carried out by a CsI(Tl) scintillating crystal array and several different germanium detectors. Each germanium detector, differing by the amount of target mass and qualities such as design and electronics, has some upsides and

downsides about threshold, noise to signal ratio and counting statistics.

HPGe An important data taking period had been carried out with a high purity germanium detector (HPGe) of 1.06 kg target mass. Data taken was in keV range with a signal threshold of 10 keV and the detector acheived a low background performance, which is essential for dark matter research, with 1 counts per (kg×keV×day) in the 12-60 keV range [11]. Results are used for setting limits on neutrino magnetic moment [11] and later on for unparticle analysis [12] and axion research [13].

CsI(Tl) CsI(Tl) detector consists of hundred 40 cm long scintillating crystals with hexagonal cross section. Readout is done by the PMTs coupled to both ends of each crystal. Total detector mass is 187 kg. Threshold for the experiment for measured electron recoil spectrum was 3 MeV. Results based on the CsI(Tl) crystal measurements include Standard Model electroweak parameters as as well as neutrino charge radius and neutrino magnetic moment. Experiment put strigent bounds on the standard model electroweak coupling constants g_V and g_A and Weinberg angle $sin^2\theta_w$. Neutrino-electron scattering cross section was also measured. This cross section calculation, in comparison to the Standard Model cross section, was used to put bounds on neutrino charge radius and neutrino magnetic moment [14]. CsI(Tl) data gave improved bounds for some of the unparticle and non-standard interaction parameters as a part of beyond the Standard Model research [12].

ULEGe An ultra low energy germanium detector (ULEGe) with 20 grams of target mass, sub-keV threshold properties and different design characteristics from above mentioned HPGe detector was used in the following data taking period. The detector collected data with low background at KSNL and an analysis threshold of 200±10 eV is achieved [15]. Results were used for WIMP dark matter analysis. Comparable results with other experiments were obtained [16].

3.2 FUTURE PROSPECTS

TEXONO is planning to carry measurements based on the subjects of neutrino-nucleus coherent scattering and dark matter research.

Neutrino-nucleus coherent scattering is a fundamental neutrino interaction which takes place in the Standard Model and it is measurable through the recoil kinetic energy of the nucleus in the detector [17].

In case of germanium detectors, this process is expected to be dominant below 1 keV recoil energy of the Ge nucleus as seen in Figure 3.1. On the other hand for typical Ge detectors, observable energy is only a fraction of the nuclear recoil energy due to quenching effects. Hence the process is not expected to be observed dominantly above few hundreds of eVs requiring lower threshold levels.

Similar situation shows itself about dark matter searches. Although considerable results have been published by the group [16], lower threshold and background levels are necessary for further improvements.

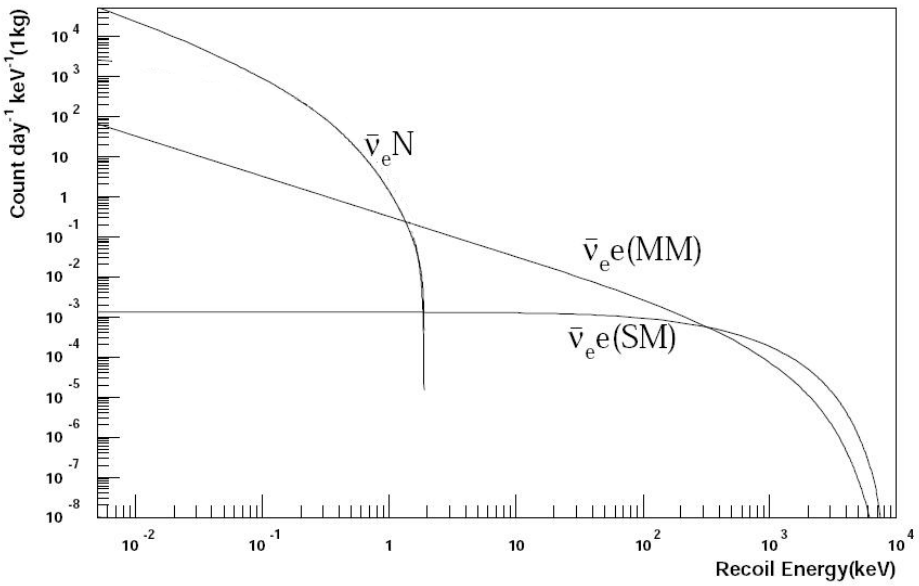

Figure 3.1: Estimated event rates of some neutrino interactions for typical germanium detectors with target mass 1 kg. Figure clearly shows the dominance of neutrino-nucleus coherent scattering process below 100 keV. Adopted from [18].

CJPL In collaboration with scientists form China, group is establishing an underground laboratory named China Jin-Ping Laboratory (CJPL). Construction works and setting up of the detector and shielding parts are already done. The laboratory has 2200 meters of rock overburden which is perfect for background purposes [18]. Above mentioned ULEGe detector

is first to take data in CJPL and it is expected to give much better results on WIMP dark matter analysis compared to its KSNL measurements due to lower background [15].

Furthermore regarding the detector techniques, group is aiming to reduce detection threshold to 100 eV with kilogram scale target mass. A 500 g point contact Ge detector (PCGe) has already taken data in KSNL and will be second to operate at CJPL. Another PCGe with 900 g target mass is taking data. Detector optimization and threshold studies are continuing.

3.3 EXPERIMENT SITE

Data taking in Kuo-Sheng Neutrino Laboratory (KSNL), which is primarily designed for reactor neutrino studies, has been conducted with several different detectors as seen in the previous sections of this chapter. In the place of data taking, this main detector is completely covered by several active and passive shielding components as seen in Figure 3.2. Active shielding components are NaI(Tl) detector, which is used to suppress γ backround, and plastic scintillator panels, which are used to suppress cosmic-ray induced background. NaI(Tl) scintillation detector, used as anti-Compton veto, is designed as a cylindrical shell, to fit a typical Ge detector in its cavity. Setup in the Figure 3.2 is sealed in a chamber into which nitrogen gas is pumped constantly to purge the air which may contain radioactive isotopes like radon which is a byproduct of uranium and thorium decay series and diffuses to air [2].

All the components seen in Figure 3.2 are placed in additional shielding structure of copper, lead, steel and boron loaded polyethylene. Boron loaded polyethylene is to eliminate the neutron background since boron, carbon and hydrogen nuclei have high neutron interaction cross sections. All the shielding structure is covered with plastic scintillator panels for cosmic-ray veto.

Data acquisition circuit for the laboratory is given in Figure 3.3, where the Ge detector is the trigger source and signals from all detector components are recorded along with the Ge signal after its trigger. All the signals from NaI(Tl) detector and plastic scintillators are used for later coincidence studies to veto anti-Compton and cosmic ray induced events.

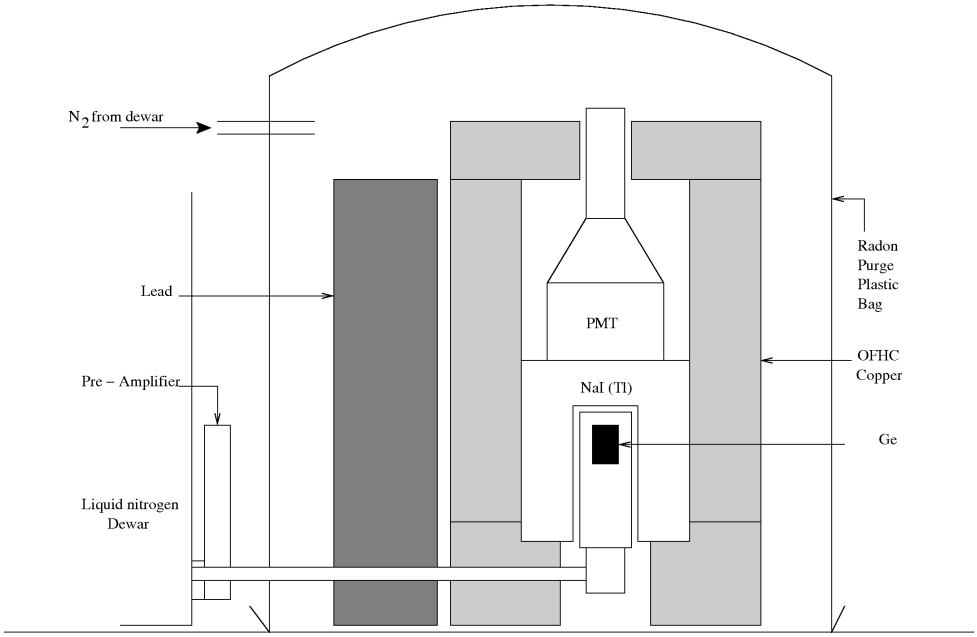

Figure 3.2: Arrangement of the detector setup at KSNL. Adopted from [11].

3.4 NEUTRON DETECTOR

In Chapter 2, it was discussed how important background studies are and how challenging problems neutron background can create. With this scope, TEXONO employed a detector uniquely to measure the neutron background in the experimental site.

Regarding the neutron background measurements in KSNL, the goal was to find the neutron background in the exact place where Ge detectors are placed. Hence a neutron detector of cylindrical shape which can exactly fit the cavity of the NaI(Tl) detector is employed for the background measurements. Neutron detector data taking period was carried out in May-June 2011 after removing the Ge detector that had been running that time and the neutron detector was placed instead. Data taking period lasted more than a month and detector gathered data of a total 43 days live time. During this period, neutron detector was the main source of trigger and anti-coincidence detectors kept running to see distribution of the neutrons with anti-Compton or cosmic-ray induced tags.

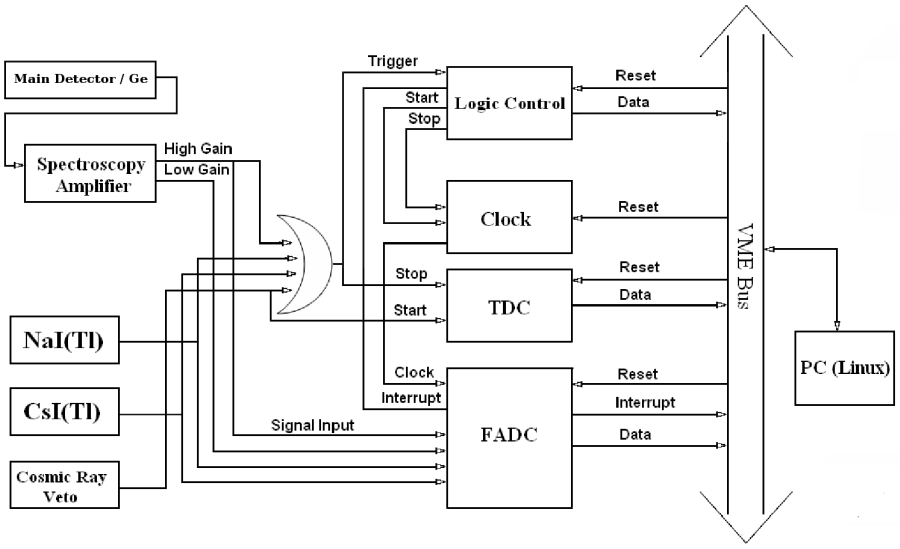

Figure 3.3: DAQ scheme for KSNL. Adopted from [19].

3.4.1 DESIGN AND CHARACTERISTICS

Neutron detector has a hybrid structure, bringing two different types of target material to operate at the same time. These materials are frequently used and well known scintillators, namely BC501A, which is sensitive fast neutrons, and BC702, sensitive to thermal neutrons.

BC501 is an organic liquid scintillator containing 4.82×10^{22} and 3.98×10^{22} atoms of hydrogen and carbon per cm^3. High density of hydrogen atoms in its compound makes it a good target material for neutron detection through neutron-proton elastic scattering for the fast neutrons in the MeV range. Detection threshold of the detector is 100 keV for recoil protons scattered by neutrons. BC501A has the pulse shape discrimination property, i.e. it yields different signals for proton and electron recoil events, enabling to distinguish neutron hit events from that of gammas [20].

BC702 is sensitive to slow/thermal neutrons, which are present in the background environment mostly as a result of moderation of the fast neutrons via elastic scattering in the shielding and other materials. Neutrons with kinetic energy below 1 eV has high neutron absorption cross-section rate in most of the nuclei. As a background source, these low energy particles will create recoils of the absorption product nuclei in detectors like Ge.

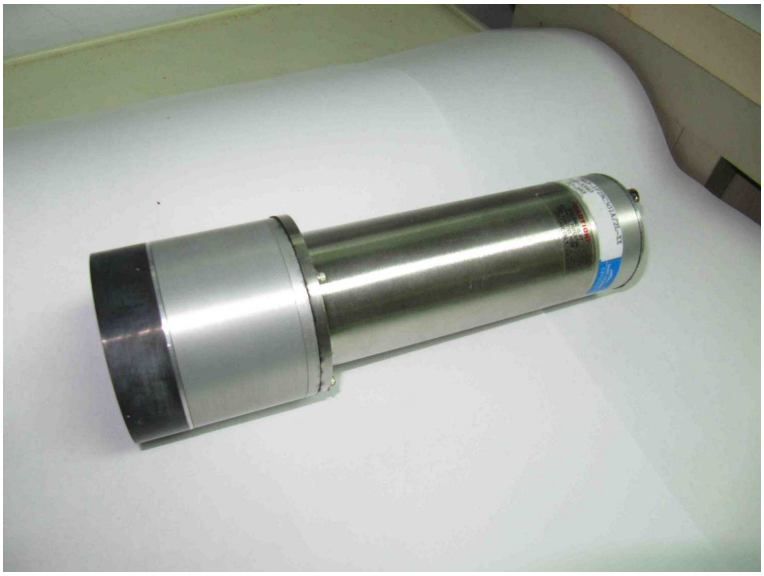

Figure 3.4: Photograph of detector used by TEXONO for neutron background measurement.

BC702 is highly efficient. Detection efficiency of neutrons with kinetic energy around 0.01 eV is above 50% and this value rapidly decreases after 1 eV. More precise efficiency calculations will be given in Chapter 5 for various neutron energies using Monte Carlo methods. Material is composed of 11 mg of ^{6}Li per cm^3 with 95% purity which is dispersed in ZnS(Ag) phosphor powder. Detection mechanism is neutron absorption by ^{6}Li

$$^6Li(n,\alpha)^3H \tag{3.1}$$

where resulting α particle and triton with recoil kinetic energy interacts with phosphor powder. Excited ZnS(Ag) molecules emit scintillation light inducing detector signal output [21].

Technical design of the detector is given in the Figure 3.5. Detector has a cylindrical design with dimensions 3.81 cm radius and 23.4 cm length. Cylindrical cells where BC501A and BC702 scintillators contained are shown with red and green colors respectively. BC501A is coupled to PMT with pyrex glass and BC702 is coupled to BC501A with an optical window (Flagged as number 6 and 8 in the Figure 3.5). Scintillating light of BC702 is transferred to PMT through this optical window and BC501A, hence scintillation light from both scintillators are collected from same optical coupling. On the other hand, scintillation output of each scintillator is different and they generate their characteristic signals. This property makes it possible to discriminate events form each scintillator.

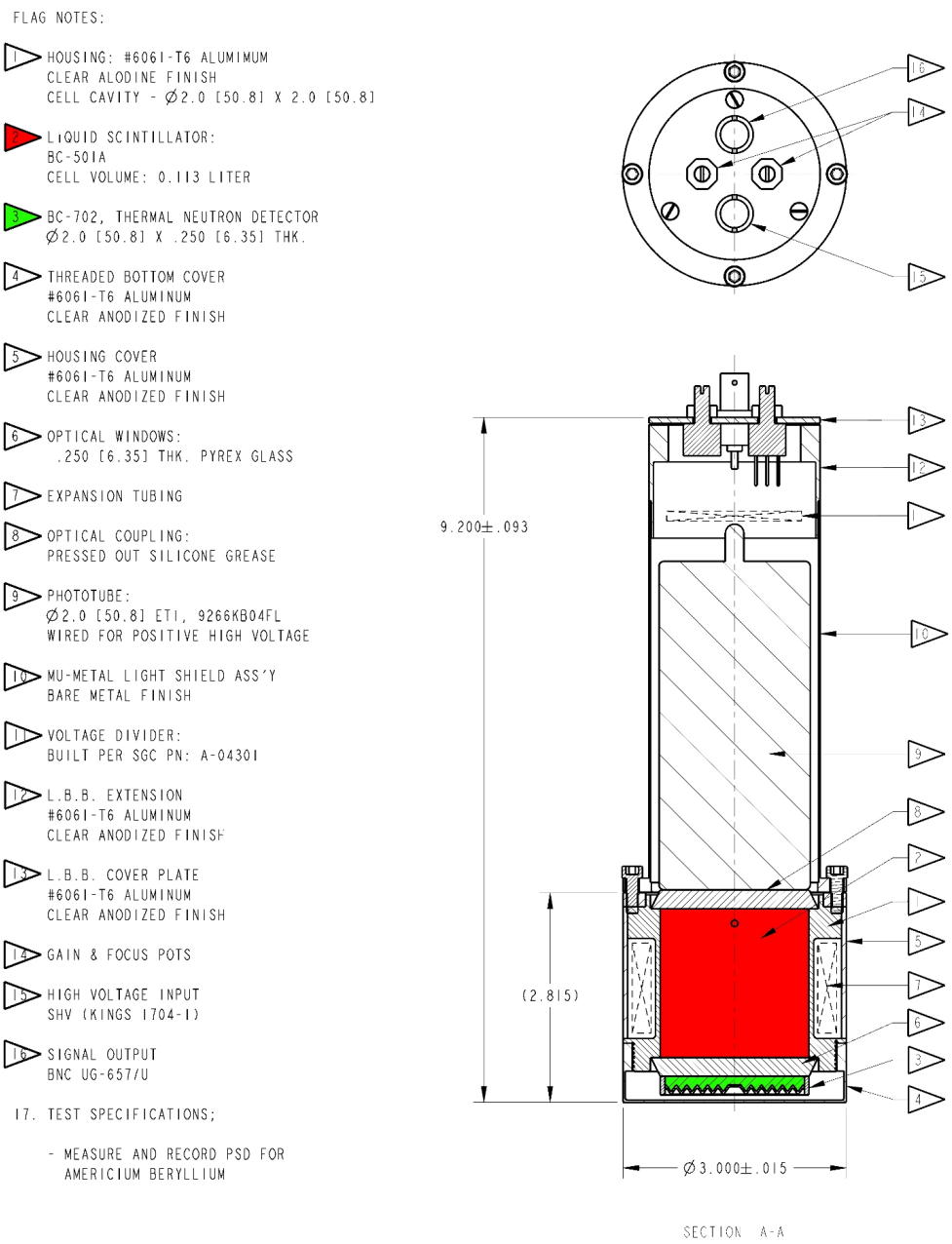

Figure 3.5: Technical Drawing of the neutron detector. Scintillators BC501A and BC702, which are the target material, are shown with red and green colors respectively. Dimensions are given in inches on the drawing.

Next sections of this chapter will try to give a complete account of detector operation principles starting from the physics processes through which beam particles are detected. Technical aspects of scintillation generation and counting will be next. Physics implications and interpretation of the collected data will follow.

3.4.2 PHYSICS INTERACTIONS

Operation principle for most of the detectors are based on generating a current from the ionization created by the charged particles passing through their target material. Hence, to fully understand the implications of the output data, it is essential to know the physics processes that can be induced by any kind of radiation incident on the detector which yields charged particles with kinetic energy in the detector. In this sense, most detectors are sensitive to gamma or X-ray radiation since they scatter off the atomic electrons of any material. Neutrons too, are sensible by most of the detectors since their probability of elastic scattering off nuclei is high, or for some elements at specific neutron energies, neutron absorption is possible.

Thermal neutrons have high cross-sections of absorption by light nuclei, especially for boron and lithium. This is why these elements are used in reactors for thermal neutron shielding along with the carbon which is used for fast neutron shielding. Cross section values at 0.025 eV thermal neutron energy are 3840 and 940 barns for boron and lithium respectively and these numbers decrease rapidly above 1 eV [22, 23, 25]. Cross section values make these elements highly preferable for slow neutron detection. Another important factor in the choice of the material is the Q-value of the nuclear reaction.

$$^{6}Li(n,\alpha)^{3}H \tag{3.2}$$

$$Q\text{–}value = 4.78\ MeV$$

$$^{10}B(n,\alpha)^{7}Li \tag{3.3}$$

$$Q\text{–}value = 2.792\ MeV$$

Q-value is the energy released in the form of kinetic energy of the daughter particles as a result of the difference in the rest masses of the initial and the final states. Although boron has higher cross-section for the reaction, lithium is also preferable for slow neutron detection since its higher Q-value which increases the detector scintillation efficiencies. Moreover, ^{10}B, has actually two (n,α) decay modes. First mode is the one with the above Q-value. It may

also decay to an excited nuclear state of ^{7}Li in which case Q-value is 2.310 MeV [22, 23, 25]. For these (n, α) reactions, kinetic energy of the incident slow neutron is negligible and has no effect in the kinematics of the reaction. Hence resulting α and triton/lithium scatters back to back.

In BC702 thermal neutron detector, ^{6}Li is dispersed in ZnS(Ag) which is a scintillating material in which recoil triton and α induces scintillation. Scintillation output for these heavy ions have characteristic long decay time. This property enables neutron signals from that of gamma events which result recoil electrons in the material [26]. Also the slow neutron events does not show an energy distribution since the total kinetic energy of the ionizing particles are constant and equal to the Q-value of the (n, α) reaction.

BC501A is an organic compound consisting of hydrogen and carbon atoms which are sensitive to neutrons via scattering. Material itself produces scintillation upon the passage of charged particles through it. Main detection channel of neutrons is neutron-proton elastic scattering. It gives scintillation response to recoil protons in the energy range between 100 keV and 100MeV. Detector is also sensitive to recoil electrons which may result from incident gamma rays. Moreover, n-p elastic scattering is not the only reaction which neutrons of MeV range kinetic energy may undergo in the detector. They may also scatter elastically from carbon nuclei, or even be absorbed by them.

BC501A has different scintillation light output characteristics for recoil electrons and heavier ionizing particles such as protons, α-particles and carbon nuclei, enabling discrimination against gamma events. After discrimination, it is possible obtain energy spectrum of the recoil nuclei induced by neutrons. Possible reaction mechanisms for fast neutrons with hydrogen and carbon nuclei are given below:

$$p(n,n)p$$
$$^{12}C(n,n)^{12}C$$
$$^{12}C(n,n+3\alpha)$$
$$^{12}C(n,\alpha)^{9}Be$$

First two reactions are elastic scattering in which incident neutron transfers some of its energy to the target nucleus. Amount of the energy transferred to recoil nucleus is determined by the initial kinetic energy of the neutron and the scattering angle of the nucleus with the relation

(for non-relativistic neutrons with kinetic energy $\ll$ 939 MeV)

$$E_R = \frac{2A}{(1+A)^2}(1 - cos\Theta)E_N \tag{3.4}$$

in the center-of-mass frame where E_N is initial kinetic energy of the neutron, E_R and A are resulting kinetic energy and mass number of the recoil nucleus and Θ is the scattering angle. In the laboratory frame, where the target particle is at rest, relation becomes

$$E_R = \frac{4A}{(1+A)^2}(cos^2\theta)E_N \tag{3.5}$$

where θ is the scattering angle of the recoil particle in the lab frame with respect to the initial neutron direction. Limits of the equation are $0 \leq \theta < 90^o$ and maximum energy is transferred to target particle for $\theta = 0$. Maximum energy that can be transferred as the percentage of initial neutron energy is thus, 100% for protons and 28.4% for carbon nuclei. As seen in Figure 3.4.2, above 1 MeV initial neutron energy, elastic scattering cross-sections from hydrogen and carbon nuclei are comparable [27].

Other two reactions are not elastic and result in alpha radiation. However, these reactions are not possible above a threshold. $^{12}C(n, n + 3\alpha)$ reaction has a threshold of 7.98 MeV. For $^{12}C(n, \alpha)^9Be$, reaction threshold is 6.17 MeV [22]. Cross-section of the later process makes a peak around 10 MeV initial neutron energy and drops to smaller values after this peak. Cross-section plots for all four processes are given in Figure 3.4.2 in the initial neutron energy range 0.1-20 MeV for comparison.

3.4.3 SCINTILLATOR AND LIGHT COLLECTION TECHNIQUES

Scintillation detectors, like all other ionization detectors, are sensitive to passage of any charged particle through them. Upon the ionization of this particle, they emit light - called scintillation. This section will try to give a brief overview of collection of this light and creating a signal current from it, as the detector output. Light emission is a result of molecular excitation of these materials and in general, amount of the photons created is related to the kinetic energy lost by the ionizing particle in the scintillating media. This property enables carrying spectroscopy studies with devices using scintillators as target material. They are used in spectroscopy of charged particles like electrons, α-partciles and protons in which case scintillation is produced directly from the ionization of the initial beam particle. On the other

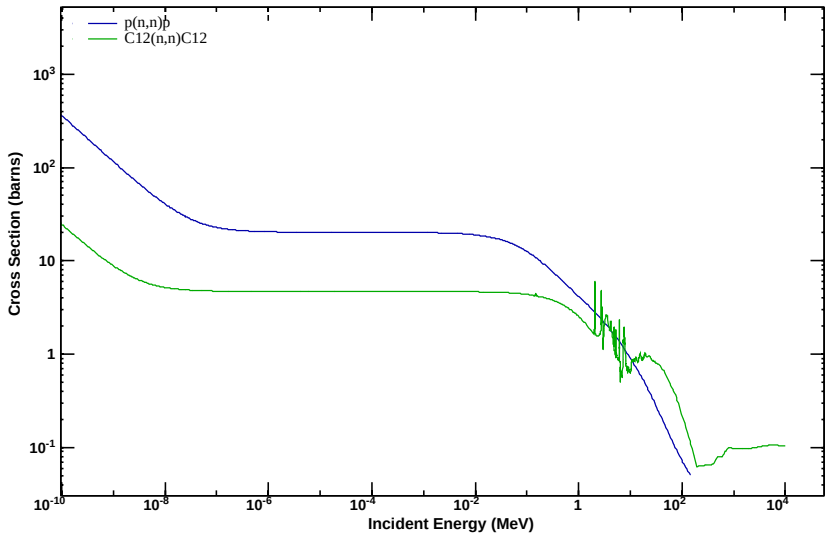

Figure 3.6: Neutron elastic scattering cross sections for protons (blue) and carbon nuclei (green). Using data from [27].

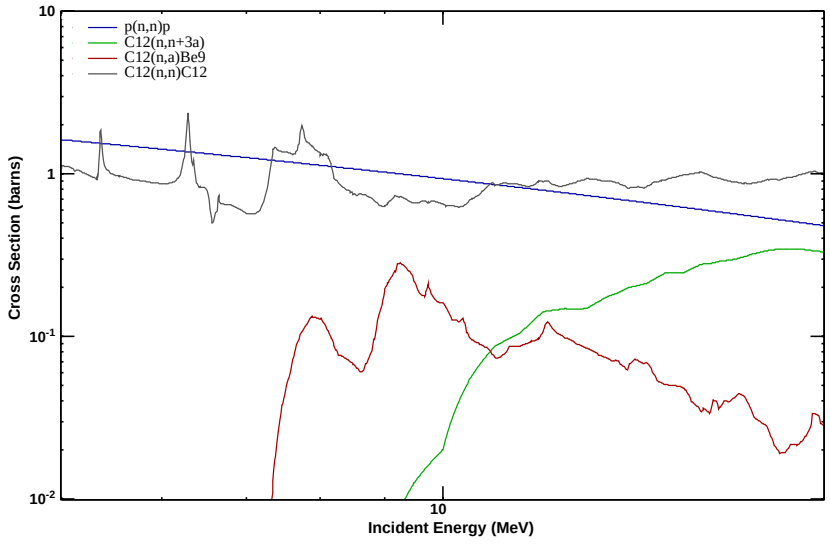

Figure 3.7: Cross sections of neutron interactions with proton and carbon nucleus. Cross section plots for elastic scattering with proton (blue), elastic scattering with carbon (black), $^{12}C(n, n{+}3\alpha)$ (green) and $^{12}C(n, \alpha)^{9}Be$ (red) are given in 5-20 MeV neutron energy interval for comparison. Using data from [27].

hand, if the beam particle is electrically neutral, scintillating material must be accompanied by a target particle which, upon its interaction with the incident radiation, will scatter in the scintillating medium causing ionization. In this respect, scintillators used in this work, BC501A and BC702 differ.

As seen in the Section 3.4.2, with BC501A, main goal is neutron detection via scattering from hydrogen and carbon. Moreover, as a hydrocarbon, BC501A itself is a scintillator. Hence the material is quiet simple, using hydrocarbon molecules both as target material and scintillating material. BC701 slow neutron detector is sensitive to slow neutrons via absorption of neutrons by lithium which result in recoil triton and α-particles. The reason that ^{6}Li is dispersed in ZnS(Ag) is just that ZnS(Ag) is phosphorescent and emits light upon the passage of charged particles.

Performance of a scintillation detector is affected by several factors but all of them can be classified under two main groups: scintillation efficiency and counting efficiency. Scintillation efficiency is related to the number of photons emitted per energy lost by the ionizing particle. This is related to the chemical properties of the scintillating material such as molecular excitation levels. Counting efficiency covers all the effects from this scintillation emission to creating a signal current as detector output.

Apart from the total number of photons emitted due to excitation, which is called absolute scintillation efficiency, photon spectrum of this emission is also important. Since, to collect the emitted photons at an edge of the material, it should be transparent to the light in its emission spectrum - emission and absorption spectra of the material should not overlap. Moreover, amount of energy lost by the ionizing particle may not be linearly proportional to the number of emitted scintillation photons, and even, this non-linear relation may be different for each type of ionizing particle. This phenomenon is called quenching and will be covered in the Section 3.4.4. Last factor in defining the scintillation efficiency is different scintillation decay time response of the materials for different types of ionizing radiation. Scintillators used in this work have this 'particle discrimination' property enabling neutron spectroscopy to be carried out. Theoretical aspects of this property and analysis methods based it will be given in the sections 3.4.5 and 4.1 respectively. In the remaining part of this section, a list of factors that contribute to the counting efficiency will be given.

All scintillation detectors should be accompanied by a photosensitive material for light count-

ing. Since the energy gaps between excited states of the scintillating molecules are few eVs, their emission spectrum is in the visible region [22, 28] and they can be detected and converted to current employing the photoelectric effect. Frequently used devices used for light collection are called photomultiplier tubes (PMT). They typically create a measurable current without much electronics noise from an input of few hundred photons. Their structure consists of a photo-cathode and an electron multiplier.

Photo-cathode is the photosensitive material coupled to an edge of the scintillating material through a transparent material like glass. When a scintillation photon reaches photo-cathode, a photo-electron is released. It migrates to the surface of the photo-cathode and escapes from there as a result of the high voltage applied to the PMT externally. Ideally this scenario predicts a photo-electron emission for each single scintillation photon reaching the photo-cathode. However, the quantity called quantum efficiency

$$QE = \frac{number\ of\ photo\text{–}electrons\ emitted}{number\ of\ incident\ photons} \tag{3.6}$$

is at most 20-30% for practical photo-cathodes. In general, few hundreds of photoelectrons are created in a scintillation event by similar amount of photons and this number is not enough to create a considerable current. Electron multiplier increases this number to 10^7 – 10^{10} electrons to create a measurable current. Finally, these electrons are collected at the anode.

Since one side of the photo-cathode is coupled to the scintillating material, photo-electrons should be collected at its other side. This is the reason why photo-cathodes should be very thin. Photoelectrons created at one side of the photo-cathode should travel in it before they reach the surface and escape to the anode side. Hence the scintillation photons should transfer enough energy to photoelectrons so that they can escape without losing all their energy in the material. But if the photon energy is too high, then photoelectrons may overcome the PMT voltage and escape to the scintillator side, rather than towards the anode. All these effects contribute to the counting efficiency of the detector [22, 28, 29].

Inefficiencies described above result in finite energy resolution of the detector. A collection of events with same energy deposition in the scintillator appear as a peak in the measured spectrum. Ideally this peak should be narrow as a Dirac Delta function at the deposited energy. In reality such collection gives a Gaussian distribution and wideness of this distribution is called the energy resolution of the detector. The role of finite energy resolution will be seen in the Chapters 4 and 5.

3.4.4 QUENCHING

In the previous section, it was shown that the process of detection of the beam particle in the scintillator involves several steps. These steps are generating secondary particles with recoil kinetic energy by the beam particle, light generation by the recoil particle in the scintillator, collecting this scintillation light at the photo-cathode and generating a signal current. Although light collection and photo-multiplication processes are not 100% efficient, the strength of the generated signal is, within the energy resolution limits of the detector, proportional to the number of the scintillation photons that reach the photo-cathode. However, number of the scintillation photons is not always linearly proportional to the energy dissipated by the recoil particle in the form of ionization or excitation, giving a non-linear signal output form the PMT. Figure 3.8 shows the typical signal strength in volts for different recoil particles with the kinetic energy E. Contrary to the linear behavior of the signal voltage of electrons, which have considerably smaller mass compared to nuclei, figure clearly represents the non-linear output from the heavier ionizing particles. Moreover, at a given recoil kinetic energy, relative light output gets lesser as the ionizing particle gets heavier.

For most of the scintillation detectors, recoil electrons with few MeV kinetic energy create a light output directly proportional to its dissipated energy. On the other hand for heavier particles, such as protons, α particles and other ions, this relation is not linear. Nonlinear behavior is first explained by Birks [30] with a semi-empirical formula which relates dissipated energy of the recoil particle per distance traveled, to the light output. This relation will be explained by following his steps in reference [28]: For a fast electron, light output L - in the form of fluorescence - is proportional to the dissipated energy E. Hence

$$L = S\,E \tag{3.7}$$

and in the differential form

$$\frac{dL}{dx} = S\,\frac{dE}{dx} \tag{3.8}$$

where S is called absolute scintillation efficiency. Linearity holds for the fast electrons since they excite individual scintillator molecules on their track which are separated and cannot interact with each other. For the same scintillating medium, dE/dx is larger for the heavier ionizing particles than the electrons of the same energy, leaving a denser ionization behind.

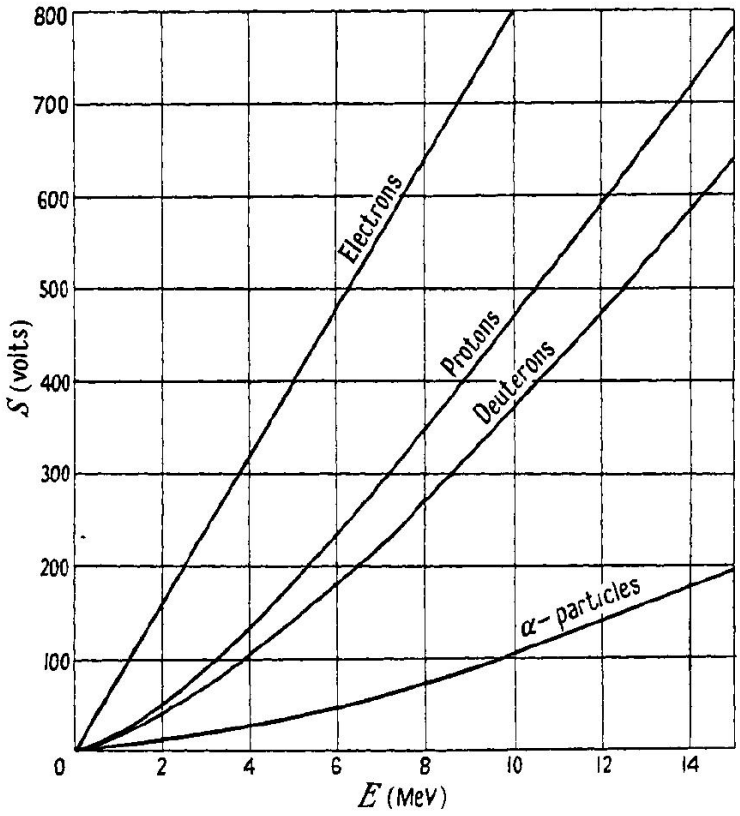

Figure 3.8: Light output functions of different ionizing particles in scintillating medium. Adopted from [30].

On the other hand, light output is below the absolute efficiency S. In general, scintillation response gets lower as the recoil particle gets heavier. This effect is called quenching.

Birks formula tries to explain this situation by imposing the term $B \times dE/dx$ to the equation 3.8 where B is a proportionality constant. Term stands for the density of the ionized or excited molecules along the track of the recoil particle and assumes as this density gets higher, interaction between molecules reduces the total light output. As modified version of the equation 3.8, Birks formula is

$$\frac{dL}{dx} = \frac{S\frac{dE}{dx}}{1 + kB\frac{dE}{dx}} \tag{3.9}$$

where k is the quenching parameter. On the limit where dE/dx is small, as in the case of fast electrons, formula reduces to equation 3.8. For large dE/dx limit, it becomes

$$\frac{dL}{dx} = \frac{S}{kB} \tag{3.10}$$

which holds for heavy ions at relatively low energies (α-particles below few MeVs) giving a light output proportional to the range of the particle (called saturation effect) [28, 30].

$$L = \frac{S}{kB}x \tag{3.11}$$

Birks proposed his formula in 1951 and it worked well since then except few discrepancies with data. Hence modified versions of his formula such as [31]

$$\frac{dL}{dx} = \frac{A}{2B}ln(1 + 2B\frac{dE}{dx}) \tag{3.12}$$

or higher order terms to his formula are proposed [32].

$$\frac{dL}{dx} = \frac{S\frac{dE}{dx}}{1 + kB\frac{dE}{dx} + C(\frac{dE}{dx})^2} \tag{3.13}$$

Both equations 3.12 and 3.13 reduce to the same behavior for small dE/dx giving the linear relation L=SE for recoil electrons. Although these formulae, especially 3.13 fit data better in most cases, they lack at predicting the saturation effect at high dE/dx.

For analysis purposes, it is necessary to know the light output of the recoil particle as a function of kinetic energy of the recoil particle in the form

$$L = L(E) \tag{3.14}$$

where L has the unit of electron equivalent energy (eVee where ee stands for electron equivalent). As an example, for liquid scintillator BC501A, which is used in this work, a recoil proton with 3 MeV kinetic energy has the same light output, thus same signal strength, with a recoil electron of kinetic energy around 1 MeV. Hence the light output of a 3 MeV recoil proton is around 1 MeVee.

Light output function for the liquid organic scintillator BC501A is provided by the producer company [20] and calculated experimentally by the works of Cecil et al. [33], Smith et al. [34] and Craun et al. [35]. There are two possible methods to measure the light output for any type of ionizing particle, direct and indirect methods. In the case of recoil protons, direct method is to bombard the detector/scintillator with monochromatic beams of protons and measure the relative light output at different beam energies. Indirect method is to use monochromatic neutron beams, which will result in recoil protons in the detector.

Edge of the spectrum in Figure 3.9 corresponds to the events with maximum light output, i.e. protons scattered back-to-back off the neutrons. Indirect method is, in general, preferred

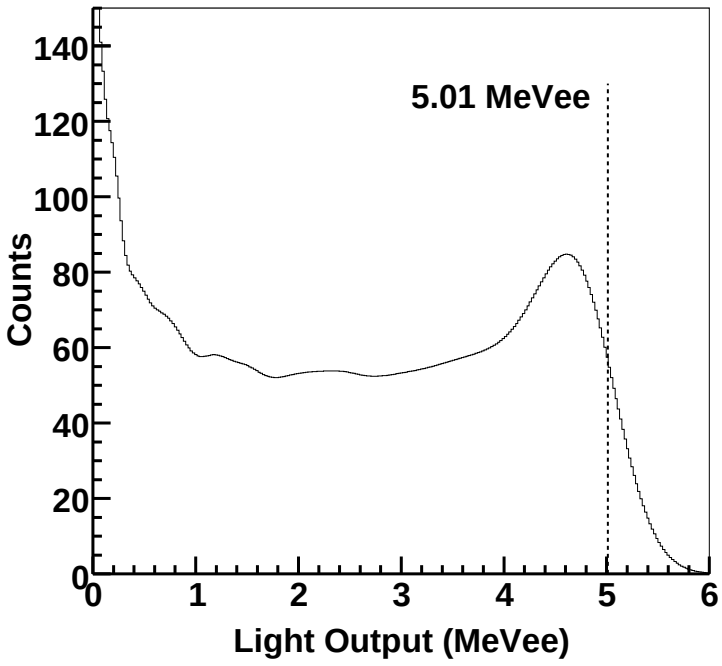

Figure 3.9: Detector response to 10 MeV neutron beam. Maximum energy edge of the spectrum corresponds to the recoil protons to which all the neutron energy is transferred via elastic scattering. (Generated using Monte Carlo as an example)

for quenching measurements. Under the influence of the neutron beam, other ionizing recoil particles such as α-particles and carbon nuclei may also be created in the detector by elastic scattering of neutrons. On the other hand, energy transfer to heavier nuclei through elastic scattering will always be less than the incident neutron kinetic energy due to energy-momentum conservation relations. Moreover, higher quenching effects for those nuclei will result a signal output, which will place such events in the low energy part of the spectrum. Thus the edge behavior of the response functions will only be determined by the proton recoil events. As an example, Figure 3.9 marks the edge at 5.01 MeVee for 10 MeV neutron beams. Generating response functions experimentally requires single energy neutron beams which can be produced in time-of-flight facilities. Without that opportunity, this work used the light output function provided by the producer company for the liquid scintillator BC501A, which is well known and used widely for neutron spectroscopy. It is obtained by Cecil et al. [33] by fitting the empirical expression 3.15 to the data by Smith et al. [34] and from other works

available at that time.

$$L(E) = A_1 \times E - A_2 \times [1 - exp(-A_3 \times E^{A_4})] \tag{3.15}$$

For the purposes of neutron spectroscopy, light output function has an essential role. As will be seen in Chapter 5, the goal of the neutron spectroscopy is to find neutron flux, namely, the energy distribution of neutrons present in the desired environment where a neutron detector will be placed. On the other hand, any detector sensitive to neutrons gives the energy spectrum of, not the neutrons itself, but recoil products in the detector. It is possible to obtain, given a recoil spectrum, the neutron flux if the response of the detector to single energy neutrons is known. Above, it was stated that it is possible to measure detector response experimentally. Due to the technical limits, to create a neutron beam at every desired energy may not be possible or feasible. Hence after experimentally determining the quenching and energy resolution of the detector system, response functions can be simulated by Monte Carlo codes which use necessary cross-section information for the reactions that can occur in the scintillator. Related to TEXONO neutron detector measurements, process of obtaining recoil spectrum is covered in the Chaper 4 and all relevant calculations and simulation studies to obtain neutron flux from recoil spectrum are given in the Chapter 5.

Recoil protons are not the only ionizing secondaries from protons. As seen in Section 3.4.2, possible secondaries include heavier nuclei such as α, ^{12}C and ^{9}Be. Therefore, while calculating the response functions, deposited energy by those recoils should also be included with their individual light output function. Especially neutrons above 8 MeV yield many α particles through ^{12}C(n,α) and ^{12}C(n,3α) reactions. For recoil α, light output function from reference [36] is adopted. Moreover, at those energies, scattering of neutrons off carbon nuclei is also very probable, and neutrons may lose considerable amount of their beam energy. On the other hand, quenching effect for this heavy ion is so high that even the highest energy ^{12}C nuclei only yield a light output below 20 keVee [37]. Soon will be shown in the Chapter 4 that threshold for the detector measurements in this work is above this value, therefore energy deposition by recoil carbon nuclei has not been included in the response function calculations.

3.4.5 PULSE SHAPE

As seen in the previous section, energy dependence of the pulse height of the signal is given by the light output function. $\frac{dE}{dx}$ dependence of the light output function is given by the Birks

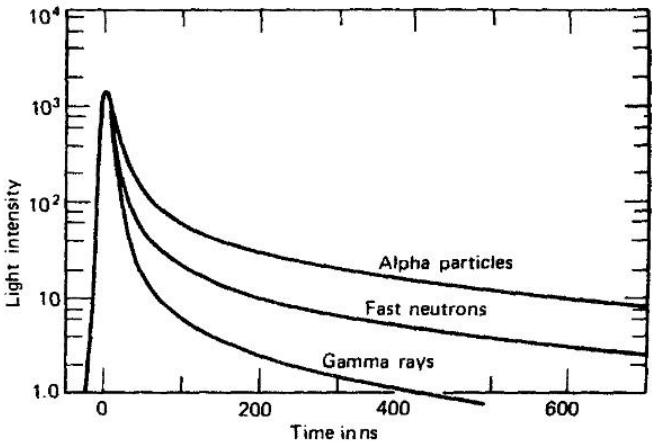

Figure 3.10: Expected time dependence behavior of signals in organic scintillators for different incident radiation. Adopted from [22].

formula (Eq. 3.13) in the previous section. Since $\frac{dE}{dx}$ differs with the nature of the ionizing particle, different ionizing particles have their characteristic light output functions. Apart from this pulse height dependence of the signal, its overall shape may also depend on the nature of the ionizing particle for some scintillating materials. In this case, a discrimination between the events from different ionizing particles is possible. Such materials with pulse shape discrimination (PSD) properties are widely used for neutron spectroscopy since the incident neutrons, different from gamma rays, are observed via some heavy ionizing particles.

Emission of the scintillation light is originated from molecular excitation and, as expected, excited levels of the scintillator molecules have lifetimes after which, they are expected to the ground state under normal conditions. Hence the light output, and the observed signal from the scintillators have time dependence. Scintillator signals, compared to the other detector technologies, are known to be vary fast, i.e. the signal reaches its peak after few tens of nanoseconds. On the hand hand, decaying time dependence of the signal is characterized by two components; a fast and in general dominant component with a decay constant of less than few tens nanoseconds, and a slow component which extends the pulse up to microsecond scale as seen in the Figure 3.10. It is the fast component of the signal which defines the total pulse height and the energy dependence as seen in the last section.

Pulse shape analysis is based on the fact that relative intensities of the fast and slow components are different for different ionizing particles [28]. For scintillators with pulse shape

discrimination property, intensity of the slow component gets higher as the ionizing particle gets heavier as seen in the Figure 3.10. Gamma radiation is always present in the environment where measurements are carried. Hence for neutron spectroscopy, it is important to isolate events induced by incident gamma radiation and leave out the neutron events.

Both scintillators used in this work, BC501A organic scintillator and BC702 slow neutron detector have pulse shape discrimination property. BC501A has a fast component with 3.14 nanoseconds decay time constant and the slowest component has a decay time of 270 nanoseconds [20]. Response of BC702 to slow neutrons, which are observed via recoil alpha particles and tritium, is unique. Fast decaying component of the BC702 (Zns(Ag)) response to heavy ionizing particles has a decay time of 200 nanoseconds, which is associated with a slower component of around 10 microseconds decay time [21]. On the other, recoil electron response of the ZnS(Ag) is thought to differ entirely from the heavy particle response, having initial fast component of less than 10 nanoseconds decay time [28].

Analysis steps based on the information given in this section will be given in the Section 4.1 showing how the detected events are separated into three groups; namely slow neutron, fast neutron and gamma events.

CHAPTER 4

DATA ANALYSIS

4.1 SIGNAL ANALYSIS AND PSD

In the Section 3.4.5, it was shown that slow neutron events from BC702 thermal neutron detector gives a signal output with a very slow decay time compared to BC501A fast neutron detector. Also BC501A signal outputs slight differ in the slow component of the the output signal for neutron and proton recoil events. Hence by analyzing the pulse shapes, it is possible to distinguish the events measured from the detector. This section will give the details of the pulse shape discrimination (PSD) technique used for the neutron detector. Three event groups with different pulse shape characteristics will be named as slow neutron events, proton-recoil events and gamma-recoil events throughout the text.

Examples of signal outputs from the detector is given in the Figure 4.1. Vertical axis of the figure corresponds to voltage output of the detector which is normalized to one. As seen in Section 3.4.5, composition of the slow and fast decay components for BC501A and BC702 differ. Light output of the BC501A is dominated by its fast component which is accompanied by a relatively weaker slow component. On the other hand, slow neutron events from BC702 has a light output response dominated by a very slow decaying component. This distinction is seen in the figure and will enable distinguishing of the signals from different scintillators. Although slow neutron signals are easy to identify, proton-recoil and electron-recoil signals from the organic scintillator only differ slightly in their slow decay component as illustrated in Figure 4.2. However it is still possible to discriminate those events completely or, if this is not possible, in the statistical limits. Below the method used to discriminate all three types of events, slow neutron, proton-recoil and electron-recoil, will be introduced. It is possible to

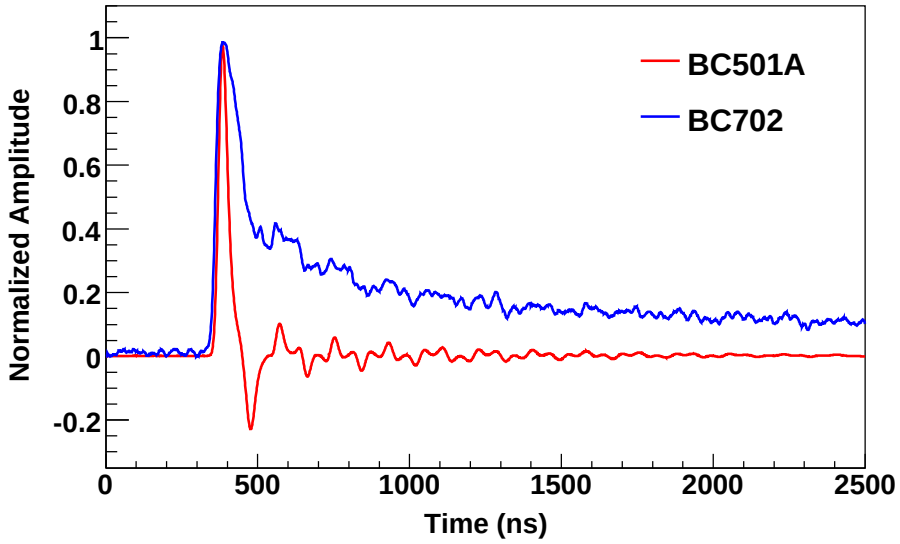

Figure 4.1: Average raw signals of events from BC501A and BC702. Vertical axis in volts is normalized to one.

discriminate events by pulse shape and it may either be done online, by using proper electronic circuits at the time of data acquisition [34, 36, 38, 39, 40], or offline, by recording all the signal information at the data taking and analyzing this information later. Both methods are based on calculating a variable using the signal information of every signal event to compare their decay behaviors. First method gives the opportunity to reject some of the gamma events while data acquisition and reduce dead time. Since expected event rate at KSNL, where neutron background was measured, is low, offline method was sufficient. There are several ways to define the PSD parameter t_{PSD}. Most basic definition is just as decay time, when the signal voltage drops below some fraction of its maximum amplitude. Since proton-recoil events decay slower, t_{PSD} for these events will be larger than those of electron-recoil events. Another method, called true pulse shape method [41], is based on comparing the signal of each event with the average signals of proton-recoil and electron-recoil events. Comparison is done by minimum χ^2-fitting event's signal to "true pulse" to find which event group they are closer. A third method, which is the most frequently used one, is based on integrating the tail region of the signal and comparing it to signals total integral. First and third methods have been tried for this work and it has been seen that the third one gives the best results. In this

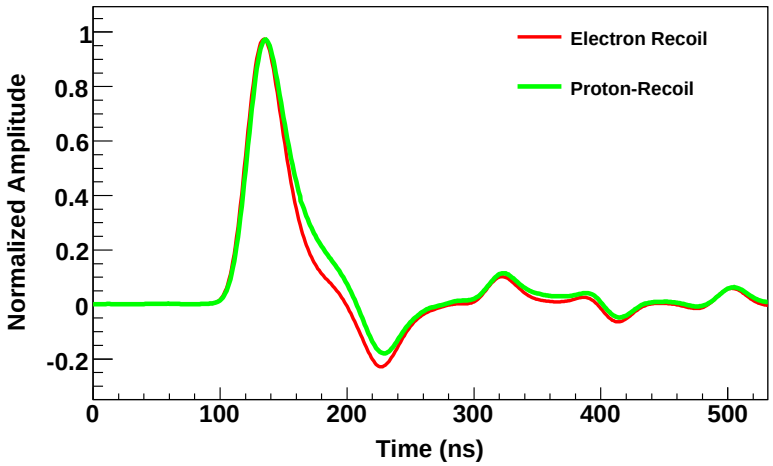

Figure 4.2: Average raw signals from the detector belonging to proton and electron-recoil events. Vertical axis in volts is normalized to one.

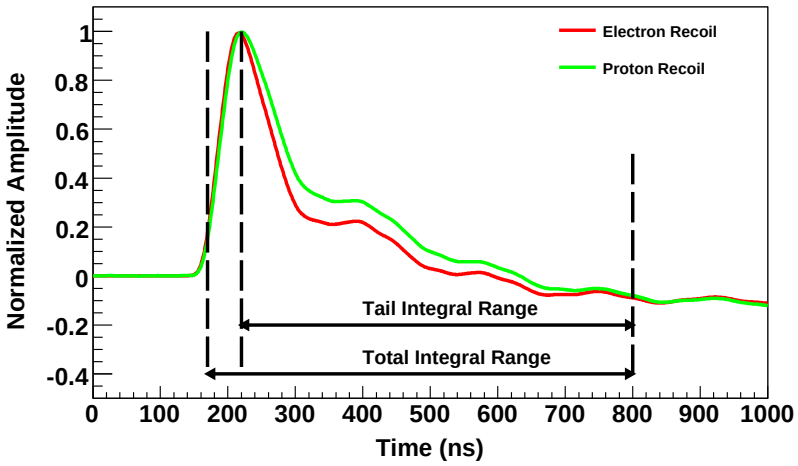

Figure 4.3: Integral ranges used to calculate PSD variable is shown on average amplified signals belonging to proton and electron-recoil events. Vertical axis in volts is normalized to one.

method, PSD variable t_{PSD} assigned to each event is calculated as:

$$t_{psd} = \frac{tail\ integral}{total\ integral} \tag{4.1}$$

where total and tail integral ranges are shown on the amplified signals in the Figure 4.3. Signals in 4.3 are same with the ones in 4.2, except they are amplified by a differential/integral amplifier to make their tail behavior stronger for better analysis. Since the rising edge behavior of the signals are same for each event, t_{PSD} value will again be smaller for electron-recoil events than those of proton-recoil events.

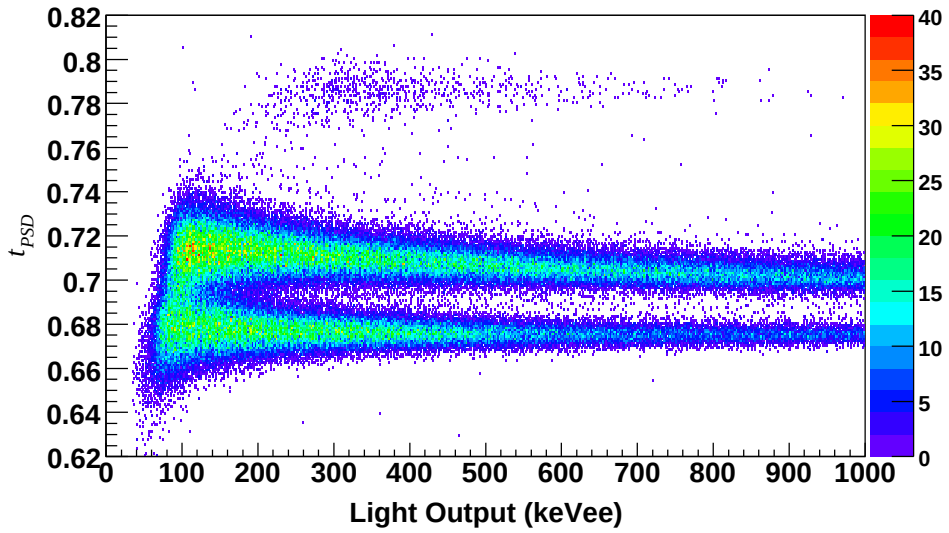

Figure 4.4: Distribution of events for PSD variable vs. light output. From top to bottom, three bands corresponding to three event groups, slow neutron, proton-recoil and electron recoil, are observed. Color scale indicates the density of events. (^{241}AmBe(α,n) source data.)

Figure 4.4 shows distribution of events for calculated PSD variable vs. light output. Data is taken while detector is exposed to radioactive ^{241}AmBe(α,n) which is a frequently used neutron source for testing performance of neutron detectors [42]. Three different bands are clear observed. The uppermost and less dense band corresponds to slow neutron events since light output of BC702 thermal neutron detector has a very long decay time. Two denser and closer bands belong to proton-recoil (middle) and electron-recoil (lower) events. Neutron emission of the source is resulted from α-capture of Be, where Am is used as the generator of α-particles needed. Slow neutron events are generally resulted from thermalization of the fast neutrons emitted by Be. In Figure 4.4, high density of the gamma band is due to

americium, which emits γ-rays along with the α-particles. Since its total emission of gammas and neutrons are in the same order, AmBe is appropriate to test the particle discrimination of the detector. In Figure 4.5 and 4.6, t_{PSD} distributions of events in different energy intervals are given where Gaussian behavior of the both event groups is evident. Separation between electron and proton-recoil events becomes very clear above 300 keV, as seen in Figure 4.6, and a complete separation between the bands is possible above this energy. Below 300 keV, as seen in Figure 4.5, although two bands are mixed, event discrimination is still possible since events follow a statistical distribution in PSD variable t_{PSD}. PSD performance can be affected by many factors in addition to the the discrimination method used [42], like detector shape, design and electronics [43]. Success of discrimination of PSD selections is represented by the quantity called figure of merit (FoM) calculated as:

$$FoM = \frac{mean_{neutron} - mean_{\gamma}}{FWHM_{neutron} + FWHM_{\gamma}} \tag{4.2}$$

FoM is simply the ratio of the distance between two mean points of the peaks in Figure 4.5 to the sum of their full width at half maxima (FWHM). For distributions with FoM greater then one, separation is considered good and yield high discrimination performance. FWHM and mean values for the peaks are obtained by fitting the following equation to t_{PSD} distribution of data:

$$\frac{A_1}{\sqrt{2\pi\sigma_1^2}} e^{\frac{-(x-x_1)}{2\sigma_1^2}} + \frac{A_2}{\sqrt{2\pi\sigma_2^2}} e^{\frac{-(x-x_2)}{2\sigma_2^2}}. \tag{4.3}$$

PSD applied to get the number of events in the proton-recoil peak has the following steps:

- Measured spectra is divided to the bins of desired number by analysis purposes.
- t_{PSD} distribution for each energy bin is drawn and FoM is calculated. Also for each bin, PSD point is determined as the minimum point of the valley between electron and proton-recoil peaks.
- Events above this determined PSD point is counted as proton-recoil.

There are two reasons for carrying PSD for each energy bin interval. First, the minimum point between the two peaks is not constant but changes with energy. Second, as shown in Figure 4.5, in low energy part, two peaks interfere. This situation necessitates correction for the selected number of events. Correction is done by estimating the number of electron-recoil

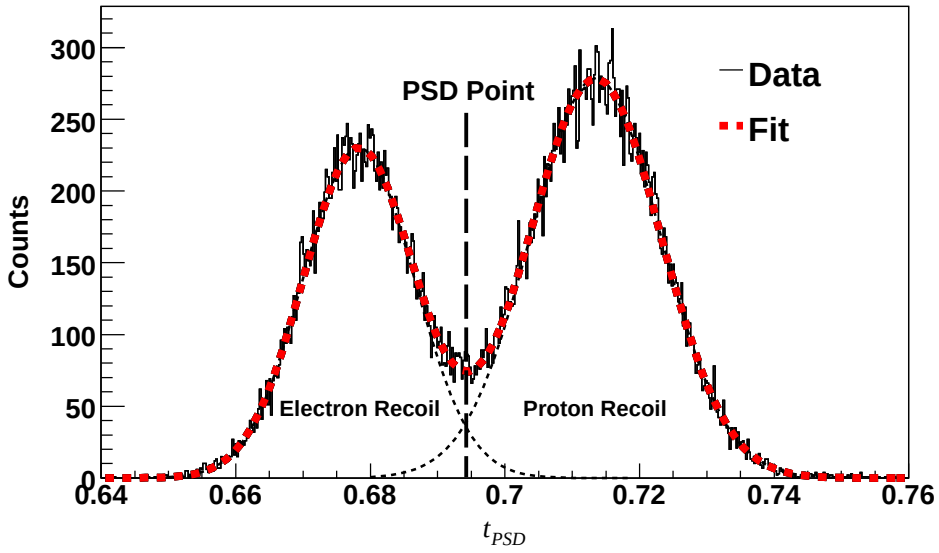

Figure 4.5: PSD variable distributions for events in the 100-200 keVee interval.

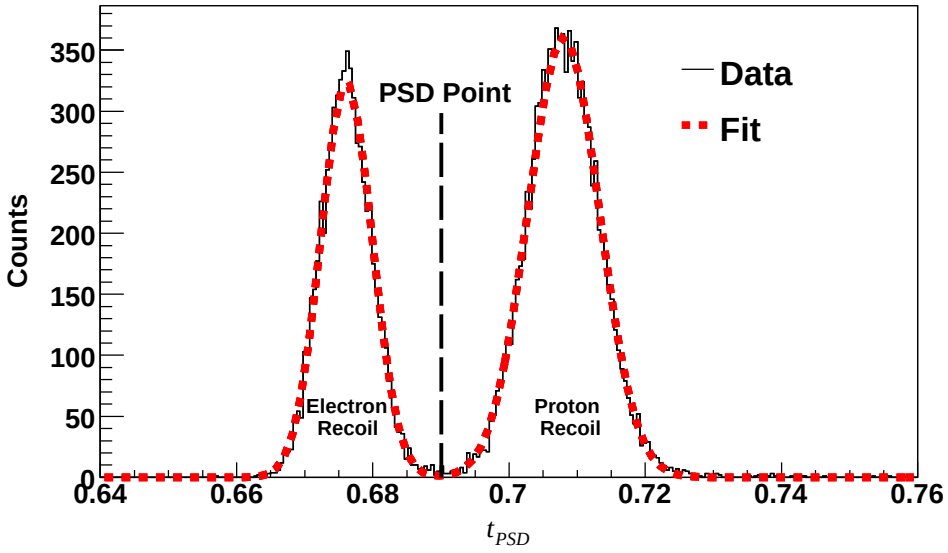

Figure 4.6: PSD variable distributions for events in the 400-500 keVee interval.

events that leak into the proton-recoil area, and proton-recoil events that leak into electron-recoil area. Leaking electron-recoil events are calculated by integrating the fitted Gaussian in the range above PSD point; and for the proton recoil events, below PSD point.

4.2 ENERGY CALIBRATION AND RESOLUTION

For energy calibration of the neutron detector, gamma sources are routinely used since detector responses to recoil electrons are linear. After this calibration process, all spectral measurements are given in terms of electron equivalent energy (eVee). It is important to note that calibration is only valid for fast neutron and gamma events observed in BC501A liquid scintillator since BC702 thermal neutron detector operates only as a counter.

Two gamma sources are used for calibration, ^{137}Cs with 661.7 keV gamma rays and ^{60}Co, with 1173.2 and 1332.5 keV gamma rays. Measured spectra while detector was exposed to these sources are given in the figures 4.7 and 4.8. Simulated electron recoil spectrum of cesium is also given in Figure 4.9 with and without including the detector resolution effect. As illustrated in the simulated spectrum, maximum energy peak of the spectra corresponds to the Compton edge, and BC501 does not shouw a full energy peak.

Peaks points of the measured spectra were determined by Gaussian fitting, and the standard deviations of the peaks were used as estimate values of the detector resolution at the corresponding energies. Calibration relation for the measurements were then obtained from the linear plot in Figure 4.10, where the data points are the peak values of the detector measurements vs. the peak points obtained from folded simulated spectrum. From the standard deviation of the peaks, resolution function parameters were also obtained as seen in the Figure 4.11.

However, there is a discrepancy between detector readings and simulated ones, as seen in the Figure 4.9. Simulated and folded spectra shows a sharper edge behavior, independent of the energy resolution values used for folding. On the other hand measured spectra extends to the full energy value of the gamma source used, which is inconsistent with the simulation and the previous experiences on BC501A [38, 44, 45, 46, 47]. This may be caused by an interference due to the gamma hits in the BC701, which is expected to be insensitive to the gamma events. This situation is further to be investigated.

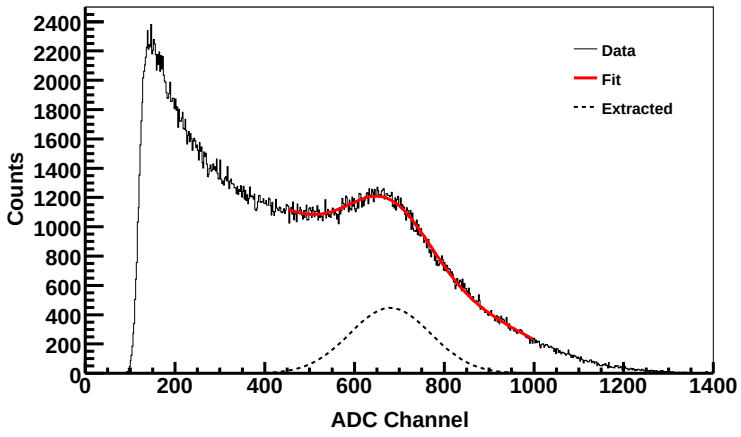

Figure 4.7: Peak of the ^{137}Cs spectrum which corresponds to the Compton edge is determined by fitting.

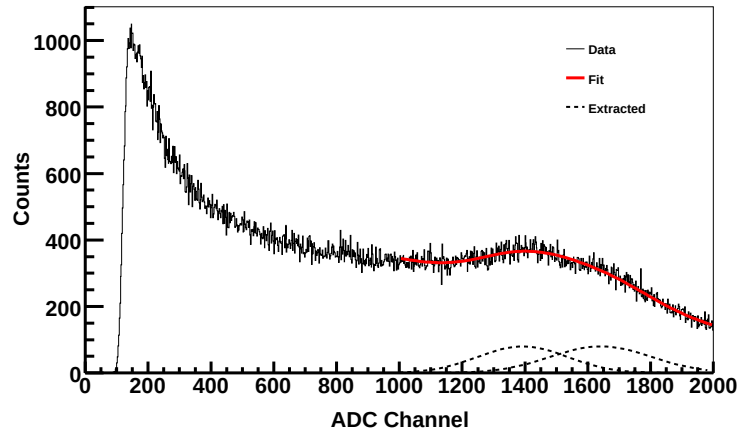

Figure 4.8: Peak of the ^{60}Co spectrum which corresponds to the Compton edge is determined by fitting.

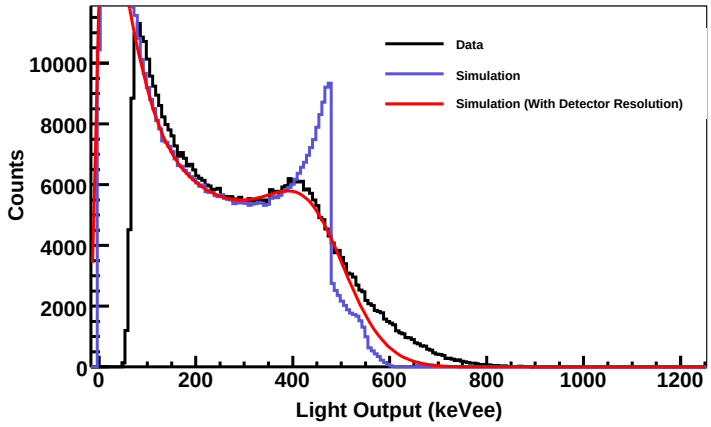

Figure 4.9: Measured ^{137}Cs spectrum is shown in comparison with the simulated recoil spectrum. Simulated spectrum after folding with detector resolution is also shown.

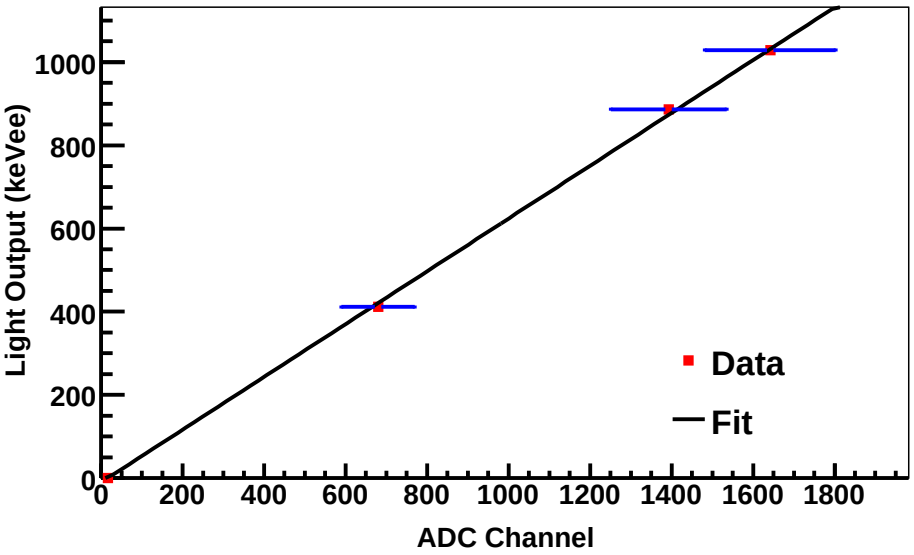

Figure 4.10: Calibration linearity plot.

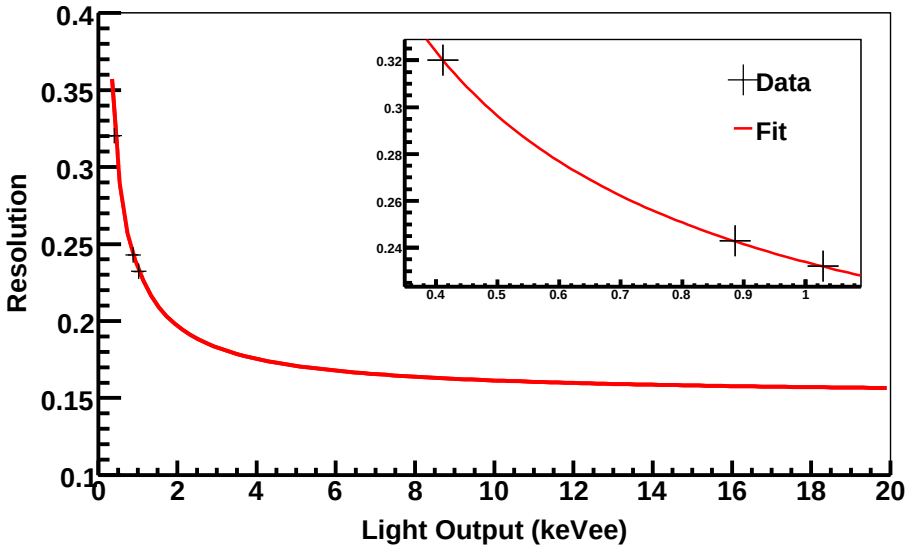

Figure 4.11: Resolution function fitted to the measured values.

4.3 PHYSICS SELECTIONS

As we have seen in Section 2.2, veto by coincidence is one of the background suppression methods. This method is based on running one or more detector systems along with the main detector and comparing the time correlation of the triggers in these secondary detectors with the main one. In this sense, TEXONO employs two veto systems in its experiment site, one is for suppressing the cosmic-induced background and the other is for gamma background.

Cosmic ray veto system is composed of an array of plastic scintillators which entirely covers the experimental setup including all other detector parts and shielding material. In case of a cosmic ray induced particle cascade during which one of the secondaries hit the main detector, it is highly probable that some of the plastic scintillator panels will also record a hit. Following this logic, if the trigger started by the main detector is in time correlation with a positive signal from one or more of these cosmic ray panels, the event is tagged as cosmic ray triggered, or CRT. Events that remain outside this category are also tagged as CRV, which stands for cosmic ray veto.

Anti-Compton veto also operates with the same coincidence principle using the signals from an NaI(Tl) scintillation detector which is highly sensitive to gamma rays. NaI(Tl) detector has cylindrical shape with a cavity. Main detector that will collect data is placed in this cavity so that any gamma ray scattering from an electron in the main detector will also pass through NaI(Tl) and deposit some of its energy here too. Hence this coincident hits, as in the case of CRT, will be tagged as anti-Compton triggered (ACT and ACV for anti-Compton veto).

During neutron data taking, neutron detector was placed in the cavity where normally Ge detectors are placed, since it is desired to know the amount of the neutron background at this exact point and data has been taken together with the coincidence detectors. Figure 4.12 shows coincident signals from NaI(Tl) detector and plastic scintillator array along with the neutron detector signal (18 microseconds apart due to electronics delay). In the events' distribution of veto timing versus neutron energy, as seen in Figure 4.13, coincident events are accumulated on the veto band which has a certain timing.

This coincidence system, however, is not perfect and its efficiency limits should be calculated. To calculate a selection efficiency, one needs a sample of events that are, for sure, should have veto tagging. For this purpose, a random trigger is generated at every 10 seconds which

starts data recording. Since this trigger is forced and not induced by a physical event, one should expect none of these events should have correlation to cosmic-ray or anti-Compton veto systems. However, it turns out that some of these events are also accidentally coincident with the cosmic-ray or anti-Compton triggers. Hence the efficiency of a veto cut is defined as the percentage of the randomly triggered events carrying the correct veto tag. For CRV and ACV cuts, efficiencies are calculated as:

$$\epsilon_{CRV} =\sim 98\%$$
$$\epsilon_{ACV} =\sim 99\%.$$

Similarly, it is also possible that a cosmic ray event may by-pass the cosmic-ray system and be counted as CRV. Ratio of this CRT events that leak into CRV set can also be estimated if there is a data sample that is cosmic induced for sure. High energy gamma rays observed in the NaI(Tl) spectrum is a good sample for this purpose, since there is no ambient source to generate gamma rays above 10 MeV other than the cosmic rays. Hence the suppression factor for CRT events (λ_{CRT}) is the fraction of CRT tagged events in this sample. Calculation yielded

$$\lambda_{CRT} =\sim 94\%$$

success rate for CRT tagging. Using these numbers, correct amount of CRT and CRV events can be estimated by

$$CRT_{real} = CRT_{measured} - CRV_{leak} + CRT_{leak} \tag{4.4}$$
$$CRV_{real} = CRV_{measured} - CRT_{leak} + CRV_{leak}$$

where CRV_{leak}/CRT_{leak} is the number of CRV/CRT events that leak into CRT/CRV set as a result of the inefficiencies as given below:

$$CRV_{leak} = (1-\epsilon)CRV_{real} \tag{4.5}$$
$$CRT_{leak} = (1-\lambda)CRT_{real}.$$

Solving equations 4.4 and 4.5 together gives the corrected CRT and CRV numbers in terms of measured ones and calculated efficiencies as follows:

$$CRV_{real}[\epsilon - \frac{(1-\lambda)(1-\epsilon)}{\lambda}] = CRV_{measured} - \frac{1-\lambda}{\lambda}CRT_{measured} \tag{4.6}$$
$$CRT_{real}[\lambda - \frac{(1-\lambda)(1-\epsilon)}{\epsilon}] = CRT_{measured} - \frac{1-\epsilon}{\epsilon}CRV_{measured} \tag{4.7}$$

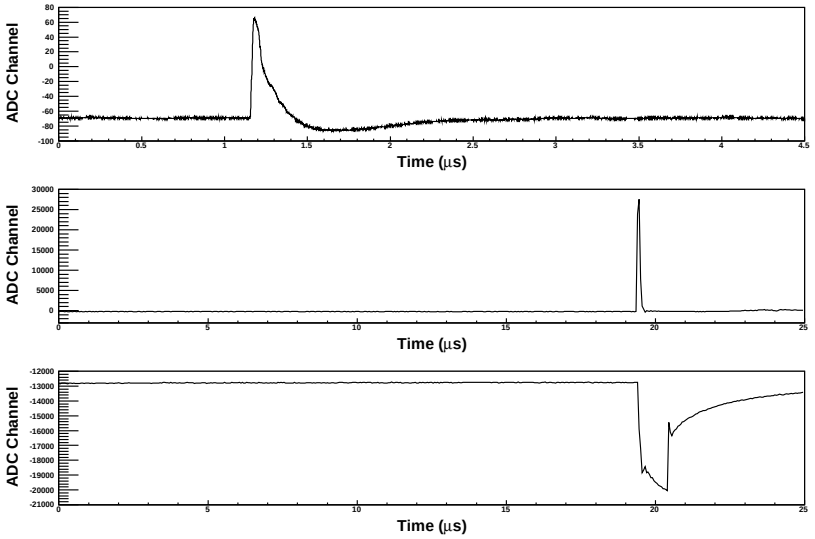

Figure 4.12: Veto signals in coincidence with the ND signal.

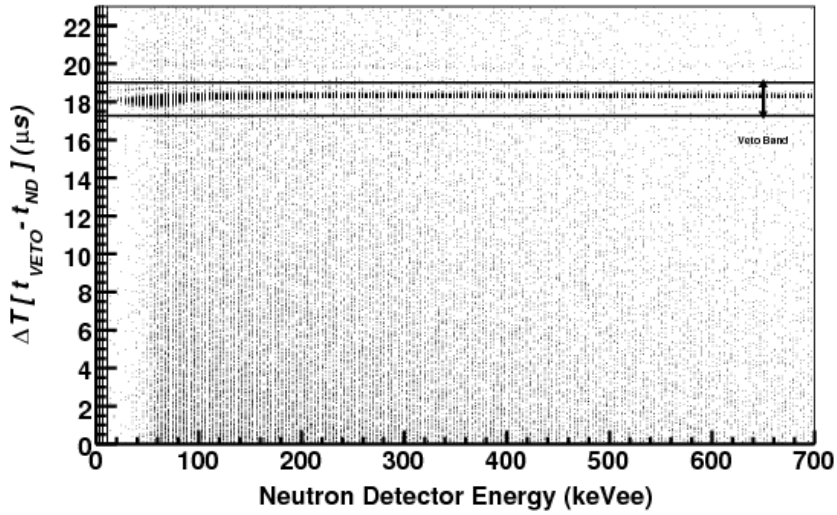

Figure 4.13: Selected band for veto events which are in coincidence with ND trigger.

CHAPTER 5

NEUTRON FLUX

In Section 3.4, it has been seen that the measured spectrum with the detector is the recoil energy spectrum of the ionizing particles. For the purposes of the neutron spectroscopy, this measured spectrum can actually be used to derive the neutron flux in the environment that the measurement has been carried out. This chapter will give an account of the techniques used to convert detector measurements into the neutron flux through some calculation methods including Monte Carlo simulation.

For a detector measurement carried under an arbitrary particle flux of $\Phi(E)$, measured spectrum $N(L)$ can be related to this flux by

$$N(L) = \int_0^\infty \Phi(E)\, R(L,E)\, dE \tag{5.1}$$

where E is the incident particle energy and L is the measured recoil energy. $R(L,E)$ in this equation is called the response function, relating the flux and the measured spectrum. Response function for a fixed E can also be considered as the measured spectrum of a monochromatic beam of incident particles at energy E, or, probability distribution of the measured recoil energy for a single incident particle with kinetic energy E. Even if this $R(L,E)$ is known exactly for a detector system, above integral equation is still not solvable for $\Phi(E)$ analytically. Furthermore, for a real measurement, equation should be in discrete form

$$N_i(L_i) = \sum_{j=1}^{J} \Phi_j(E_j)\, R_{ij}(L_i, E_j) \tag{5.2}$$

$$i = 1, ..., I$$

$$j = 1, ..., J.$$

and finding $\Phi_j(E_j)$ requires using a computational method called unfolding (or deconvolution) which is widely used in neutron spectroscopy and dosimetry applications. Hence first of all,

response functions should be determined to solve the problem. Most straightforward method for obtaining response functions is to measure the recoil spectra for monochromatic neutrons at every beam energy E_j. Also, if the energy resolution and light output functions of the detector is known, response functions can also be calculated by Monte Carlo methods as will be seen in the later sections of this chapter.

5.1 MONTE CARLO METHODS

For all Monte Carlo calculations carried within this work, *GEANT*4 Monte Carlo code [48] is used. *GEANT*4 provides the necessary cross section data for the processes that may occur through the simulated physical situation. Its working principle is based on tracking the primary particle in the created environment that has been shot by the user, and its secondaries, through each step which corresponds to a physical process (interaction). Then at each step, desired information for the process (like energy, interaction type, daughter particles etc.) can be recorded for later analysis. Next two sections will give basic information on the entire process of the simulation used for calculating response functions.

5.1.1 DESIGN OF THE GEOMETRY

Any detector measurement is not only determined by the incident particles but also detector geometry, particle beam alignment and even the configuration of the surrounding materials. Hence for the most realistic case, all the detector components and the surrounding materials in the real data taking environment is included in the design of the simulation, as seen in the Figure 5.1. Main components in the design are the neutron detector itself located in the cavity of the NaI(Tl) detector and the surrounding copper shielding. All the materials are specified with their atomic composition.

5.1.2 RECORDING EVENT INFORMATION

In reality, signal generation form the neutron detector, as outlined in Section 3.4, is resulted from scintillation light collected by PMT, and this scintillation light is induced by ionizing recoil particles. The relation between this light output and the energy lost by ionization has been

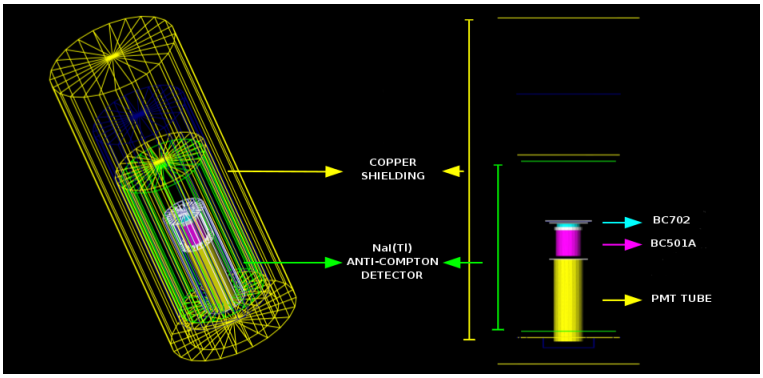

Figure 5.1: Geometric design of the simulation where copper shielding and NaI(Tl) anti-Compton detector surrounding the neutron detector is shown.

discussed in the section on quenching. Hence in the simulation, physics processes following incidence of a beam neutron are tracked only up to the energy loss of ionizing secondaries, and scintillation light generation is not included in the simulation. Instead, expected signal output form an ionizing event is calculated using the light output function for the specific recoil particle.

Information for the secondaries of each particle type following an incident neutron is recorded in the event information if there is an energy loss by ionization in the volume of one of the scintillating materials. As we have seen in the Section 3.4.2, possible ionizing secondaries induced by fast neutrons are recoil protons, α-particles and carbon nuclei, along with possible electrons, positrons and any other nuclei that may be created by rare nuclear reactions.

Considering an ambient background, it is expected that distribution of the background particles should not have any direction dependence, i.e. they should be randomly distributed in space. Since scope of this work is to measure the background in the exact position in which Ge detectors are placed in the simulation incident neutron particles were created in the volume inside the NaI(Tl) detector with a random position and direction distribution, to imitate the real case as much as possible.

For each incident neutron, energy deposition information is recorded regarding to three categories:

- Type of the particle that deposited energy

- Material in which energy is deposited
- Physical process that resulted in energy deposition

Above information is recorded only if energy is deposited in one of the scintillator materials, BC501A and BC702, and if energy is deposited by an electrically charged particle through ionization since scintillators produce light due to ionization. Data is recorded separately for different material and different particle type. For example, if an incident γ-ray is generated, it is possible that it may interact multiple times with the electrons in the scintillator media and scatter them via Compton scattering. At each scattering, a recoil electron is created which later deposits its energy through ionization. This information is recorded by summing the deposited energies of each electron for that event. Since for electrons, as seen in Section 3.4.4, deposited energy is linearly proportional to the signal output voltage, energy spectrum of measured and simulated spectrum will be the same without any additional effect. This situation does not hold for heavier recoil particles and quenching effect should be considered while comparing simulation with real data. Light output functions for recoil protons and α-particles in BC501A fast neutron detector is shown in Figure 5.2

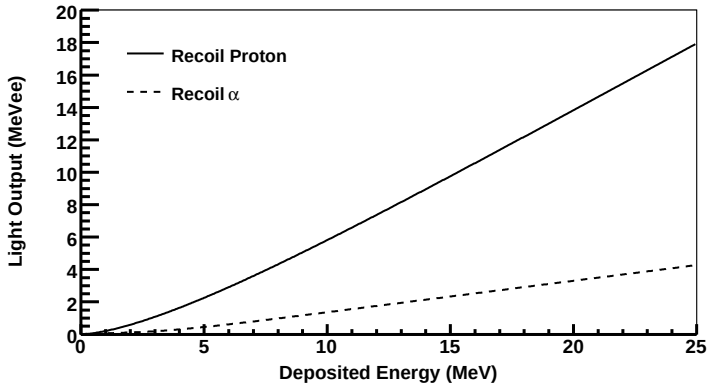

Figure 5.2: Light output functions for recoil protons [20] and α-particles [36, 45] in BC501A liquid organic scintillator.

In case of incident neutrons with multiple interactions, each recoil secondary like proton and α-particle, will deposit their energy in the scintillator at macroscopically separated areas, hence, energy deposition by each secondary should be factorized by the light output function at the deposited energy.

5.2 GENERATING RESPONSE FUNCTIONS

To obtain the fast neutron flux using the signal information from BC501A, response function in the equation 5.2 should be calculated. As seen in Section 3.4.2, possible recoils that can be induced by fast neutrons in BC501A fast neutron detector was protons, α-particles and carbon nuclei. Response functions $R_{ij}(L_i, E_j)$ were generated by Monte Carlo, by creating a neutron beam of 1 million particles at energy E_j and obtaining the light output spectrum L of recoil particles. Energy deposition by carbon nuclei was ignored due to their high quenching, i.e. relatively low light output compared to their energy deposit.

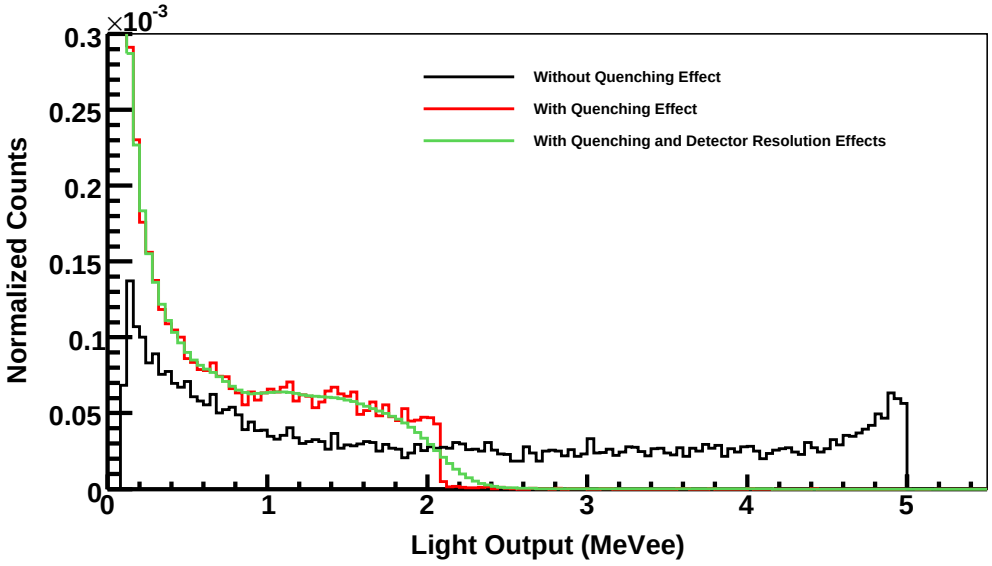

Figure 5.3: Calculated detector response to 5 MeV neutron beam (green). Simulated energy deposition by proton and α-particles without and with quenching effects are plotted with black and red colors respectively. After folding red spectrum with detector resolution, green spectrum (response function $R(L, E)$ at $E = 5MeV$) is obtained.

Figure 5.3 shows the procedure for calculating a response function $R_{ij}(L_i, E_j)$ at a specific neutron energy E_j. Comparison of black and red spectra shows the effect of quenching, since red spectrum is obtained by counting the energy of recoil events after multiplying with proper light output functions. Red spectrum is obtained by distributing each bin content of the red spectrum with a Gaussian whose FWHM at each specific light output L_i is given by

the resolution function

$$\frac{FWHM(L)}{L} = \sqrt{A^2 + \frac{B^2}{L} + \frac{C^2}{L^2}}. \tag{5.3}$$

Hence for a specific neutron energy of incidence E_j, i^{th} component of the response function is calculated by the following relation

$$R_{ij}(L_i, E_j) = \sum_{k=1}^{K} \int_{L_i-\Delta L}^{L_i+\Delta L} \frac{C_k}{\sqrt{2\pi\sigma^2(L_k)}} e^{\frac{-(L'-L_k)^2}{2\sigma^2(L_k)}} dL' \tag{5.4}$$

$$i, k = 1, ..., I.$$

where L_i is the light output value of the response function bin whose content is wanted to be calculated. Contribution from each Gaussian distributed bin of the red spectrum at L_k is integrated in the i^{th} interval $L_i \pm \Delta L$. C_k is the content of the k^{th} bin of the red spectrum. $\sigma(L)$ is calculated from the resolution function 5.3 using the relation

$$\sigma(L) = \frac{FWHM(L)}{2.35} \tag{5.5}$$

Examples of response functions at several energies between 1 and 8 MeV E_j is given in the Figure 5.4.

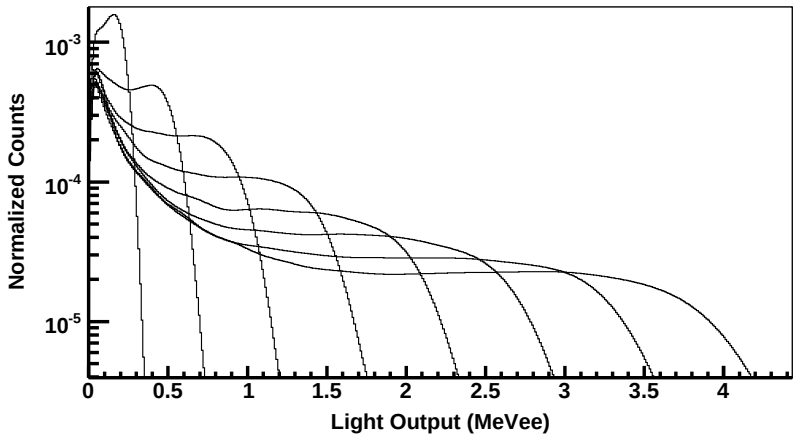

Figure 5.4: Calculated response functions $R(L, E)$ at $E = 1,\ 2,\ 3,\ 4,\ 5,\ 6,\ 7,\ 8\ MeV$

For calculation of the neutron flux $\Phi(E_j)$, these response functions are calculated at 1000 neutron beam energies E_j between 0 and 20 MeV.

5.3 SIMULATED EFFICIENCY

Efficiency of the detector can also be calculated by using Monte Carlo simulation. Calculations have been done by counting the fraction of detected events for neutron beams at different energies of incidence. Results are given in this section in two categories, slow neutron detection efficiency of BC702 slow neutron detector through the interaction

$$^{6}Li(n,\alpha)^{3}H \tag{5.6}$$

and fast neutron detection efficiency of BC501A fast neutron detector at neutron beam energies from 0 to 20 MeV.

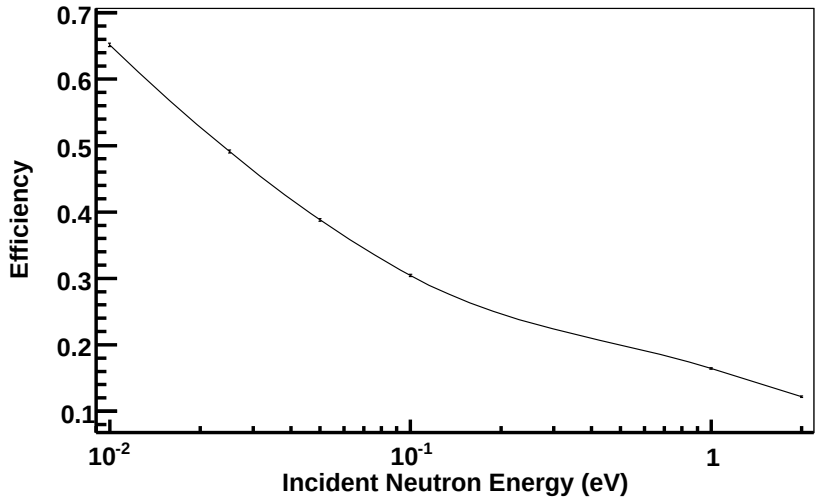

Figure 5.5: Simulated efficiency of BC702 at several slow neutron energies.

Figure 5.5 shows the calculated efficiency values at slow neutron energies from 0.01 eV to 2 eV. Results are consistent with the numbers provided by the producer company of BC702 [21].

Fast neutron detection efficiency has been calculated at 1000 neutron beam energies up to 20 MeV and for different detection energy threshold settings. Calculations have been done at each neutron beam energy by counting the fraction of the detected events whose light output is greater than the given threshold value. Curves in figure 5.6 from top to bottom give the calculated efficiencies without threshold, 60 keV threshold, 100 keV threshold and 1 MeV

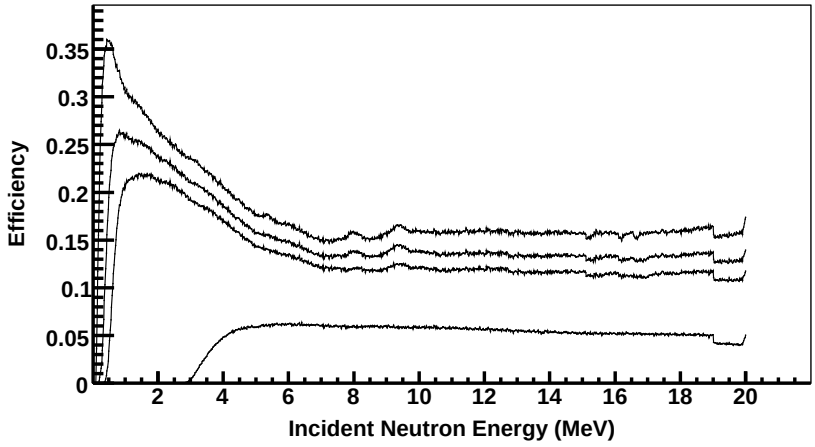

Figure 5.6: Simulated efficiency of BC501 with respect to incident neutron energy. Different curves belong to different threshold settings. Uppermost curve is for no threshold. Others are, from top to bottom, at threshold values at 60 keV, 100 keV and 1 MeV.

threshold respectively. It is possible to find similar calculations of efficiency for BC501A in the literature. Calculated values of this work are consistent with the previous works who provide similar results of efficiency calculated by Monte Carlo, or measured experimentally [33, 49].

5.4 UNFOLDING

After calculating the response functions, this section will give an outline of the computational method used to calculate the neutron flux $\Phi(E)$ from the detector measurements. Unfolding, or deconvolution, is a widely used computational method in neutron spectroscopy. Method had been developed primarily for neutron dosimetry measurements for radiation protection purposes at nuclear facilities or similar environments where it is of crucial importance to know the abundance of the neutron radiation [50, 51]. There are several computational algorithms for unfolding. This work uses one developed by Doroshenko et al. [52], which calculates the neutron flux by an iterative method. Algorithm is simply:

$$\Phi_j^{n+1} = \frac{\Phi_j^n}{\sum_{i=1}^{I} R_{ij}} \sum_{i=1}^{I} R_{ij} \frac{N_i}{\sum_{k=1}^{I} \Phi_k^n R_{ik}}. \tag{5.7}$$

Algorithm calculates the j^{th} bin of the neutron flux $\Phi_j(E_j)$. Index n over the Φ indicates the iteration number. Algorithm work with the inputs $N_i(L_i)$, detector measurement, and

response function $R_{ij}(L_i, E_j)$ and an initial neutron flux $\Phi_j^0(E_j)$. This initial flux is just to get the algorithm started, but if there is a strong guess on the expected neutron flux, it may fasten up the calculations, or even may result in more precise result [53]. In general, few hundreds of iterations are enough for calculation to converge, and good fitting is obtained.

CHAPTER 6

RESULTS

6.1 AmBe MEASUREMENTS

For testing detector performance and correctness of calibration and PSD performances, detector had been exposed to a well known fast neutron source. Figure 6.1 and 6.2 respectively gives the measured recoil spectrum and unfolded flux from the recoil spectrum respectively. For comparison, unfolded spectrum is given with measurement of a similar work [54] which is consistent with other measurements of the AmBe neutron flux [44, 54, 55, 56, 57] and the theoretical calculation of Geiger and Van Der Zwan [58]. As seen in the Figure 6.2, there is a discrepancy between the measurements of this work and the others. However, obtained result is consistent about the positions and relative intensities of the peaks of the spectrum. Discrepancy may result from several reasons. Calibration and energy resolution values obtained in the previous chapters have primary importance and may need correction. Also data taking setup may lead unexpected variations in the measurements, although the geometric setup had been tried to be simulated with the most realistic consideration. Measurement with AmBe source in this work was carried by placing the source and the detector in a lead shielding. Moreover, detector and the source were in close proximity. Since AmBe emits gamma rays along with the neutrons, this choice of the experimental setup may have been resulted in hits of multiple particles at the same time. Any of the above mentioned factors which may have failed to be estimated exactly will results an uncertainty in the response functions, thus in the final unfolded flux.

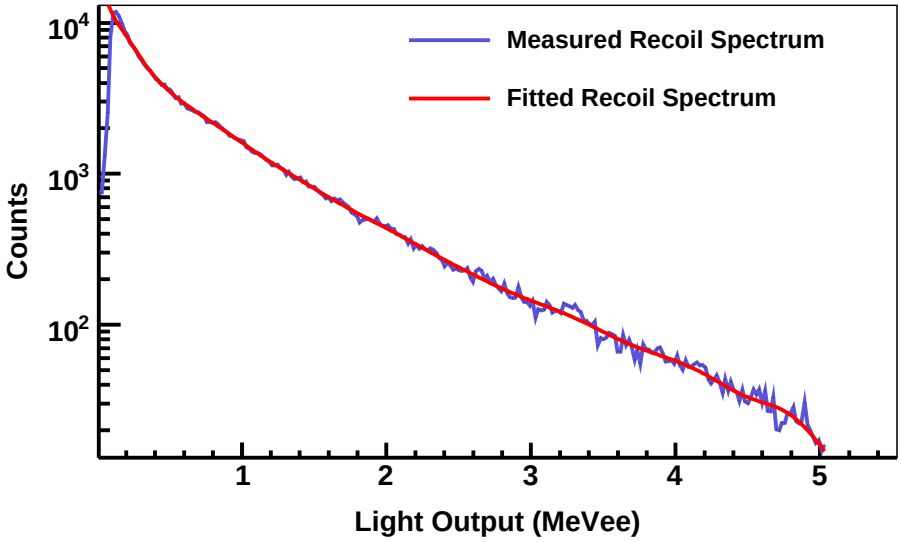

Figure 6.1: Measured recoil spectrum of AmBe source.

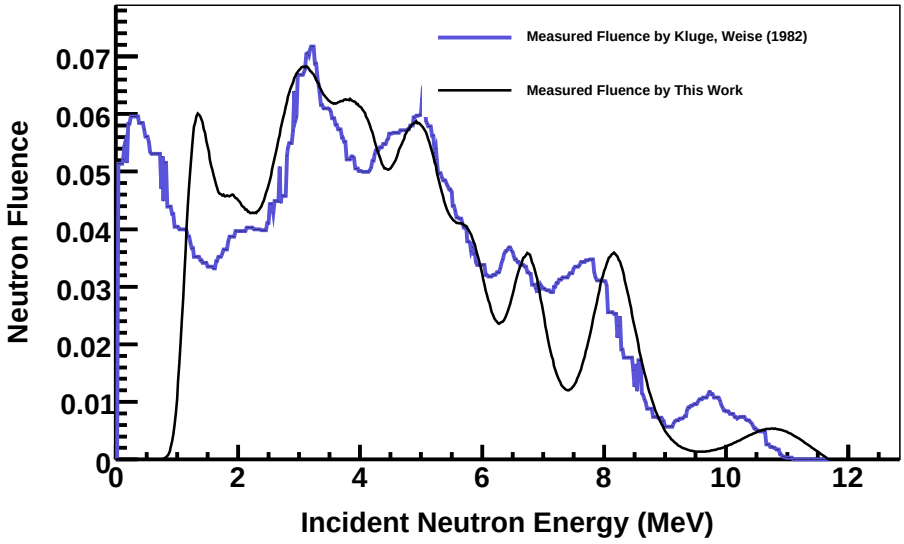

Figure 6.2: Measured neutron fluence of AmBe source given in comparison with the measurement of Kluge and Weise (1982) [54]. Two spectra are normalized to equal number of detector counts.

6.2 KSNL MEASUREMENTS

Measurements carried in the Kuo-Sheng Neutrino Laboratory will be given in this section in two parts, fast neutron flux and thermal neutron flux. Fast neutron flux measurements for each physics selection as discussed in the Section 4.3 will be given along with the corresponding recoil spectrum in the first part. Second part will give the calculational steps which leads to thermal neutron flux from the counts of BC702.

6.2.1 FAST NEUTRON FLUX

For different physics selections using different coincidence tags, neutron flux has been obtained by unfolding corresponding recoil spectrum. Tags are:

- RAW - Without any selections, spectrum of all events
- CRT&ACT - events that are coincident both in cosmic ray and anti-Compton veto systems
- CRV&ACV - events that are not coincident both in cosmic ray and anti-Compton veto systems
- CRT&ACV - cosmic ray tagged, but not coincident with anti-Compton veto
- CRV&ACT - only coincident with anti-Compton veto.

For comparison, fluxes with five different selection cuts are given on the same plot in Figure 6.3. Measured recoil spectrum corresponding to the curve “ALL” is also given in the Figure 6.4. Success of the unfolding is given by the grey curve in Figure 6.4, which is actually the exact response of the calculated flux. Other measured spectra and the unfolded flux corresponding to each physics selection are also given in the Figure 6.2.1.

6.2.2 SLOW NEUTRON FLUX

Slow, or thermal neutrons are below 1 eV kinetic energy particles and their source is slowing of faster neutrons down to an energy distribution which is in thermal equilibrium with the

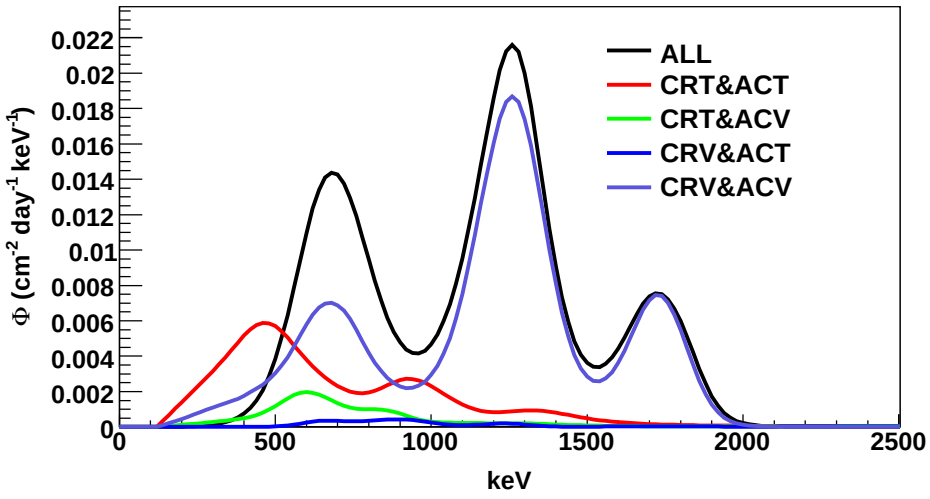

Figure 6.3: Unfolded neutron fluxes for 5 different selections.

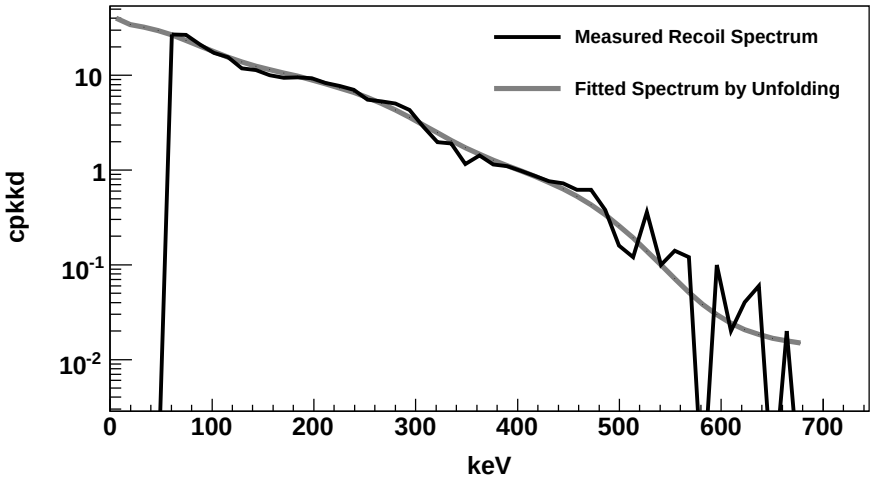

Figure 6.4: Detector reading without any selection cuts. Neutron flux obtained by unfolding this recoil spectrum is given in the upper panel with the label ALL.

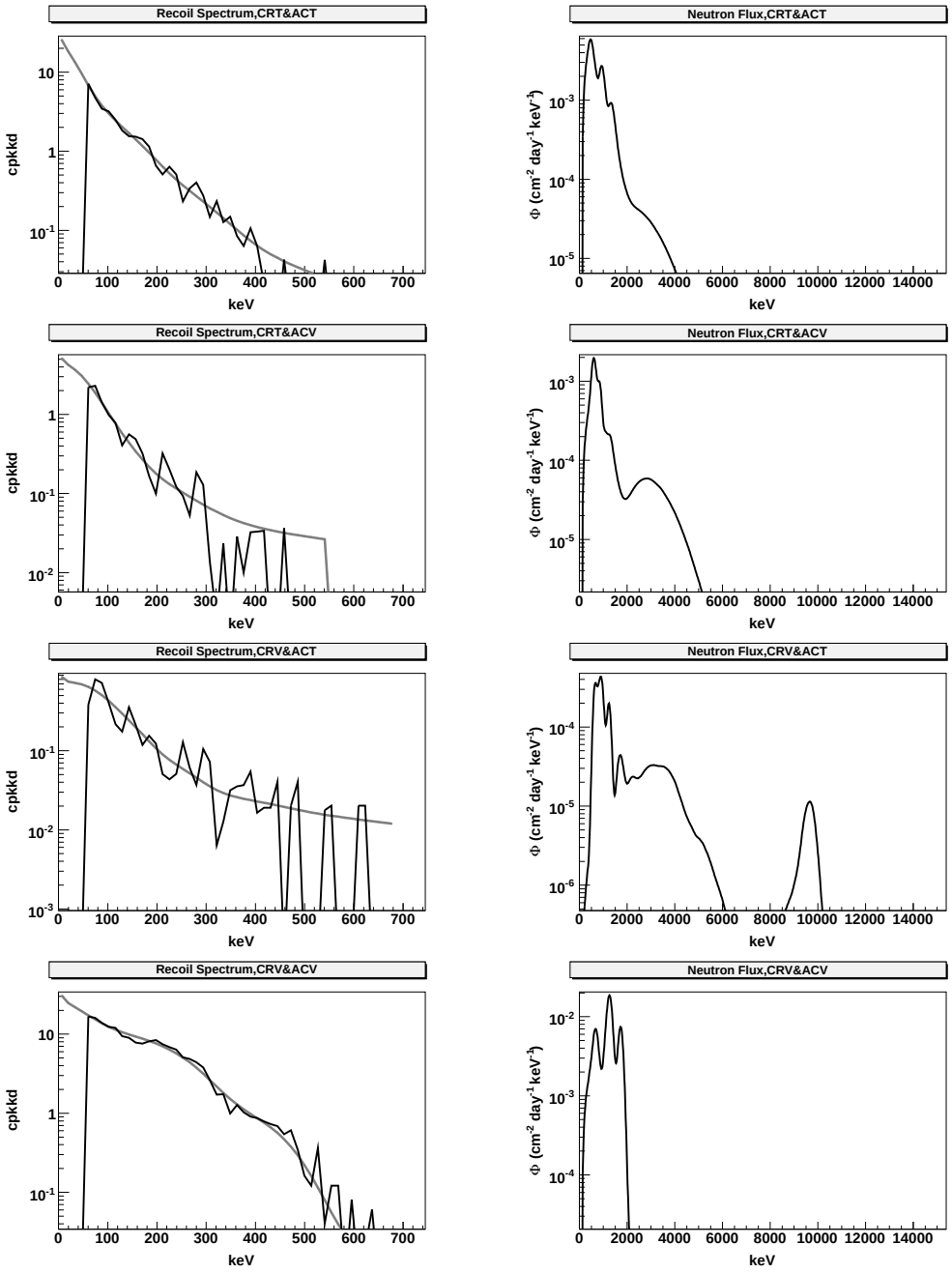

Figure 6.5: Measured recoil spectra and neutron flux for different selection cuts.

surroundings. Energy distribution of these particles show a Maxwell-Boltzmann distribution with the most probable energy 0.02 eV (corresponds to a velocity of 2200 m/s), which is known as the thermal neutron energy. Since the scintillator BC702, which is used for thermal neutron measurements, gives no energy information related to the incident thermal neutrons, flux calculations are done by assuming Maxwell-Boltzmann distribution holds.

For a flux $\phi(E)$ of particles with interaction cross-section $\sigma(E)$ in the detector, number of counts in the detector per second is

$$C = N \int_0^{E_{max}} \sigma(E)\phi(E)dE \tag{6.1}$$

where N is the total number of target nuclei in the detector. It is known that (n,α) reaction cross-section for ^6Li is proportional to the inverse of the neutron velocity $v(E)$ [59] and it can be written as

$$\sigma(E) = \sigma_0 \frac{v_0}{v(E)} \tag{6.2}$$

where v_0 is a neutron velocity at which reaction cross-section σ_0 is known. Moreover, for an isotropic and homogeneous distribution, flux can be written as

$$\phi(E) = v(E)n(E) \tag{6.3}$$

where n(E) is the density of neutrons in the detector volume and the count rate is written in terms of total number of the neutrons in the volume as

$$C = N\sigma_0 v_0 n. \tag{6.4}$$

Considering the average neutron velocity and the total flux

$$\bar{v} = \frac{\int v(E)n(E)dE}{\int n(E)dE} = \frac{\phi}{n} \tag{6.5}$$

rate becomes

$$C = N\sigma_0 \frac{v_0}{\bar{v}}\phi. \tag{6.6}$$

For thermal neutrons, which has Maxwell-Boltzmann distribution, average velocity is $\bar{v} = 2v_t/\sqrt{\pi}$ where v_t is the most probable thermal neutron speed 2200 m/s [60]. Since neutron capture rate for lithium at thermal neutron energy is known to be 940 barns, total flux and rate are related as

$$C = N\sigma_t \frac{\sqrt{\pi}}{2}\phi \tag{6.7}$$

$$\phi = \frac{2C}{N\sigma_t \sqrt{\pi}}. \tag{6.8}$$

Measured slow neutron count rate at KSNL with BC702 is $3.44 \pm 0.10 \times 10^{-4}$. With a total number of 1.25×10^{22} lithium atoms in BC702 [21], total neutron flux in the Maxwell-Boltzmann distribution is

$$\phi = 3.30 \pm 0.10 \times 10^{-5} neutrons\ cm^{-2}\ s^{-1} \tag{6.9}$$

REFERENCES

[1] R. J. Gaitskell, Annu. Rev. Nucl. Part. Sci. 2004. 54:315-59.

[2] G. Heusser, Annu. Rev. Nucl. Part. Sci. 1995. 45:543-90.

[3] J. A. Formaggio, C. J. Martoff, Annu. Rev. Nucl. Part. Sci. 2004. 54:361-412.

[4] V. Tomasello, V.A. Kudryavtsev, M. Robinson, Nuclear Instruments and Methods in Physics Research A 595 (2008) 431-438.

[5] Dongming Mei, A. Hime, Phys.Rev. D73 053004 (2006). [arXiv:astro-ph/0512125v2]

[6] M. J. Carson, J. C. Davies, E. Daw, R. J. Hollingworth, V. A. Kudryavtsev, T. B. Lawson, P. K. Lightfoot, J. E. McMillan, B. Morgan, S. M. Paling, M. Robinson, N. J. C. Spooner, D. R. Tovey, Astroparticle Physics Volume 21, Issue 6, (2004) 667-687. [arXiv:hep-ex/0404042v1]

[7] M. J. Carson et al., Nuclear Instruments and Methods in Physics Research A 546 (2005) 509-522.

[8] M. Robinson, New Astronomy Reviews 49 (2005) 315-321.

[9] L. Stodolsky, Astroparticle Physics 35 (2011) 114-118.

[10] V. Chazal, R. Brissot, J. F. Cavaignac, B. Chambon, M. De Jesus, D. Drain, Y. Giraud-Heraud, C. Pastor, A. Stutz, L. Vagneron, Astroparticle Physics 9 (1998) 163-172.

[11] H.B. Li et al. (TEXONO Collaboration), Phys.Rev.Lett. 90 (2003) 131802. [arXiv:hep-ex/0212003v2]

[12] M. Deniz et al. (TEXONO Collaboration), Phys. Rev. D 82, 033004 (2010). [arXiv:hep-ex/1006.1947]

[13] H. M. Chang et al. (TEXONO Collaboration), Phys. Rev. D 75, 052004 (2007). [arXiv:hep-ex/0609001v2]

[14] M. Deniz et al., (TEXONO Collaboration), Phys. Rev. D 81, 072001 (2010). [arXiv: hep-ex/0911.1597]

[15] H. T. Wong et al., Nucl. Phys. A 844, 229c (2010).

[16] S. T. Lin et al., (TEXONO Collaboration), Phys. Rev. D 79, 061101(R) (2009). [arXiv:0712.1645v4]

[17] D. S. Freedman, Phys. Rev. D 9 1389 (1974).

[18] H. T. Wong, H. B. Li, J. Li, Q. Yue and Z. Y. Zhou, J. Phys. Conf. Ser. 39 (2006) 266. [arXiv:hep-ex/0511001]

[19] M. Deniz (2007). *Measurement of SM Electro-Weak Parameters in Reactor Antineutrino-Electron Scattering in TEXONO Experiment* (Ph. D. Thesis). Retrieved from http://etd.lib.metu.edu.tr/upload/12608386/index.pdf.

[20] Saint-Gobain Crystals, BC-501, BC-501A & BC-519 Liquid Scintillator Product Data Sheet, Retrieved from http://www.detectors.saint-gobain.com/document.aspx?docId=201818, June 2012.

[21] Saint-Gobain Crystals, BC-702 Thermal Neutron Detector Product Data Sheet, Retrieved from http://www.detectors.saint-gobain.com/document.aspx?docId=201854, June 2012.

[22] G. F. Knoll, Radiation Detection and Measurement, 3rd Ed., John Wiley & Sons, Inc., New York, 2000.

[23] B. T. Price, C. C. Horton, K. T. Spinney, International Series of Monographs on Nuclear Energy, Div. 10, Vol. 2: Radiation Shielding, Pergamon Press, 1957.

[24] J. B. Marion, J. L. Fowler, Fast Neutron Physics Part 1: Techniques, Interscience Publishers, 1960.

[25] J. B. Marion, J. L. Fowler, Fast Neutron Physics Part 2: Experiments and Theory, Interscience Publishers, 1963.

[26] R. Stedman, Rev. Sci. Instrum. 31, 1156 (1960).

[27] Brookhaven National Laboratory, National Nuclear Data Center, http://www.nndc.bnl.gov/, January 2012.

[28] J. B. Birks, The Theory and Practice of Scintillation Counting, Pergamon Press, 1964.

[29] W. L. Leo, Techniques for Nuclear and Particle Physics Experiments, Springer-Verlag, Berlin, 1987.

[30] J B Birks, Proc. Phys. Soc. A 64 874 (1951).

[31] G. T. Wright, Phys. Rev. 91 1282 (1953).

[32] C. N. Chou, Phys. Rev. 87 904 (1952).

[33] R. A. Cecil, B. D. Anderson, R. Madey, Nuclear Instruments and Methods, 161 (1979) 439-447.

[34] D. L. Smith, R. G. Polk, T. G. Miller, Nuclear Instruments and Methods 64 (1968) 157-166.

[35] R. L. Craun, D. L. Smith, Nuclear Instruments and Methods 80 (1970) 239-244.

[36] H. Klein, Radiat. Prot. Dosimetry. (2003) 107 (1-3): 95-109.

[37] S. Yoshida et al., Nuclear Instruments and Methods in Physics Research A 622 (2010) 574-582.

[38] F. Arneodo, et al., ICARUS Collaboration, Nuclear Instruments and Methods in Physics Research A 418 (1998) 285-299.

[39] F. T. Kuchnir, F. J. Lynch, IEEE Transactions on Nuclear Science, Vol. 15, No. 3, June 1968.

[40] M. Moszynski et al., Nuclear Instruments and Methods in Physics Research A 350 (1994) 226-234.

[41] C. Guerrero et al., Nuclear Instruments and Methods in Physics Research A 597 (2008) 212-218.

[42] Z. Cao, L. F. Miller, Nuclear Instruments and Methods in Physics Research A 416 (1998) 32-44.

[43] F. Begin, G. Assaillit, J. E. Groetz, Nuclear Instruments and Methods in Physics Research A 562 (2006) 351-357.

[44] Wang Song-Lin, Huang Han-Xiong, Ruan Xi-Chao, Li Xia, Bao Jie, Nie Yang-Bo, Zhong Qi-Ping, Zhou Zu-Ying, Kong Xiang-Zhong, Chinese Physics 33(5) (2009) 378-382.

[45] H. Klein, S. Neumann, Nuclear Instruments and Methods in Physics Research A 476 (2002) 132-142.

[46] A. Ohrn, Nuclear Instruments and Methods in Physics Research A 592, Issue 3, p. 405-413.

[47] G. Dietze, IEEE Transactions on Nuclear Science, Vol. NS-26, No. 1, February 1979.

[48] S. Agostinelli et al. Nuclear Instruments and Methods in Physics Research A 506 (2003) 250-303.

[49] HUANG Han-Xiong, ZHOU Zu-Ying, NIE Yang-Bo, RUAN Xi-Chao, LI Xia, CHEN Guo-Chang, BAO Jie, ZHONG Qi-Ping, Chinese Physics 33(8) (2009) 667-681.

[50] Neutron monitoring, Proceedings of the Symposium on Neutron Monitoring for Radiological Protection, International Atomic Energy Agency, Vienna, 1967.

[51] Neutron Monitoring for Radiation Protection Purposes; Proceedings of a Symposium on Neutron Monitoring for Radiation Protection Purposes, International Atomic Energy Agency, Vienna, 1973.

[52] J.J. Doroshenko, S.N. Kraitor, T.V. Kuznetsova, K.K Kushnereva and E.S. Leonov, Nuclear Technology 33 (1997) 296-304.

[53] H. R. Vega-Carrillo, M. P. I. Torre, Nuclear Instruments and Methods in Physics Research A 476 (2002) 270-272.

[54] H. Kluge, K. Weise, Radiat. Prot. Dosimetry. (1982) 2 (2): 85-93.

[55] A. Zimbal, Radiat. Prot. Dosimetry. (2007) 126 (1-4): 413-417.

[56] N. Magalotti et al., Radiat. Prot. Dosimetry. (2007) 125 (1-4): 69-72.

[57] M. Flaska, S. A. Pozzi, Nuclear Instruments and Methods in Physics Research A 577 (2007) 654-663.

[58] K. W. Geiger, L. Van Der Zwan, Nuclear Instruments and Methods, 131 (1975) 315-321.

[59] D. J. Hughes, International Series of Monographs on Nuclear Energy, Div. 2, Vol. 1: Neutron Cross Sections, Pergamon Press, 1957.

[60] N. Tsoulfanidis, S. Landsberger, Measurement and Detection of Radiation, 3rd Ed., CRC Press, 2010.